Computers in Biology and Medicine 196 (2025) 110695

Contents lists available at ScienceDirect

Computers in Biology and Medicine

journal homepage: www.elsevier.com/locate/compbiomed

In silico screening of a designed focused chemical space identifies novel alkyl hydrazides as potent HDAC11 inhibitors

Fady Baselious [a], Sebastian Hilscher [a], Lukas Handke [a], Cyril Barinka [b], Mike Schutkowski [c], Wolfgang Sippl [a,*]

[a] Department of Medicinal Chemistry, Institute of Pharmacy, Martin-Luther-University of Halle-Wittenberg, Halle (Saale), Germany
[b] Institute of Biotechnology of the Czech Academy of Sciences, BIOCEV, 252 50, Vestec, Czech Republic
[c] Charles Tanford Protein Center, Department of Enzymology, Institute of Biochemistry and Biotechnology, Martin-Luther-University of Halle-Wittenberg, 06120, Halle (Saale), Germany

ARTICLE INFO

Keywords:
HDAC11
Virtual screening
Classification model
AlphaFold
Docking
Molecular dynamics simulation
Alkyl hydrazides

ABSTRACT

The therapeutic potential of HDAC inhibitors containing a hydroxamic acid moiety as a zinc-binding group (ZBG) is limited in clinical use due to their potential mutagenicity. In addition, hydroxamic acids often exhibit off-target effects that can lead to undesirable toxicity. Therefore, the development of HDAC inhibitors with alternative ZBGs has proven to be a promising approach to overcome these drawbacks. HDAC inhibitors carrying alkyl hydrazide as ZBG have recently been published as selective inhibitors for different HDAC subtypes. In the present study, a ligand-based virtual screening workflow, employing a classification categorical model, was developed and applied for a designed targeted chemical space. The two most promising hits from the virtual screening were synthesized and evaluated by in vitro enzyme inhibition assays. Both hits showed strong inhibition of HDAC11 with IC_{50} values in the nanomolar range. In addition, the compounds showed good selectivity towards HDAC11 at a concentration of 1 μM, only HDAC8 was also significantly inhibited among all tested subtypes. Finally, the binding mode of the selected candidates was investigated by docking against different HDACs, followed by molecular dynamics simulations and metadynamics studies to provide insights for further chemical optimization.

1. Introduction

Histone deacetylases are enzymes that catalyze the removal of acyl groups from acylated lysine residues of various histone and non-histone proteins [1]. The members of this family can be classified into class I (HDAC1-3 and 8), class IIa (HDAC4, 5, 7 and 9), class IIb (HDAC6 and 10), class III (Sirt1-7) and class IV (HDAC 11) [2]. While most HDAC subtypes preferentially remove acetyl groups, HDAC11 is distinguished by its ability to remove longer fatty acyl groups.

HDAC11 is the smallest member of the histone deacetylase family, and its catalytic domain constitutes approximately 80 % of the protein sequence [3,4]. Several studies demonstrated that HDAC11 is implicated in various biological and pathophysiological conditions. For example, it plays a role in immune system modulation, particularly in the regulation of the type I interferon signaling pathway [5]. Additionally, it has been reported to act as a repressor of interleukin-10 transcription [6]. HDAC11 messenger RNA was found to be overexpressed in many cancer cells [3] and its overexpression in pituitary and liver cancer cells was negatively correlated with the expression of the tumor suppressor p53 [7,8]. Furthermore, several studies [9–11] have investigated the link between HDAC11 and obesity development. It has been demonstrated that knocking out (KO) HDAC11 can protect against hyperlipidemia and weight gain. Additionally, it can enhance glucose tolerance, alleviate insulin resistance, and reduce hepatic steatosis [12].

To date, only a few potent and selective hydroxamic acid-based HDAC11 inhibitors have been reported [13]. FT895, an isoindoline derivative [13], has shown efficacy in combating lung cancer [14]. Another inhibitor, PB94, features a methoxy group substitution in the ortho position of the benzohydroxamic acid moiety along with a bulky adamantane moiety. PB94 demonstrated beneficial effects in neuropathic pain mouse model [15]. In a previous study, we reported the development of a selective HDAC11 inhibitor with a novel scaffold that showed promising activity on the BE2C neuroblastoma cell line [16]. Furthermore, we identified another selective inhibitor by applying a comparative structure-based virtual screening approach using an optimized AlphaFold2 model of HDAC11 [17].

* Corresponding author.
E-mail address: wolfgang.sippl@pharmazie.uni-halle.de (W. Sippl).

https://doi.org/10.1016/j.compbiomed.2025.110695
Received 13 March 2025; Received in revised form 12 June 2025; Accepted 29 June 2025
Available online 4 July 2025

HDAC11 has been attributed with a preferred de-fatty acylase activity, indicating the presence of a so-called "foot pocket" that can accommodate longer alkyl chains [5,18–20]. Taking advantage of this structural feature of HDAC11, selective inhibitors bearing long alkyl chains were developed, such as the alkyl hydrazide derivative SIS17 [21] and the trapoxin A analogue TD034 [22]. However, both compounds exhibit unfavorable drug-like properties that limit their bioavailability.

The hydroxamic acid zinc-binding group (ZBG) is a well-characterized pharmacophore for chelating the zinc ion and is the most commonly used ZBG in the development of HDAC inhibitors [23,24]. Several hydroxamic acid HDAC inhibitors have been approved by the FDA for clinical use [25], such as vorinostat for cutaneous T-Cell lymphoma [26], belinostat for peripheral T-cell lymphoma [27] and panobinostat for multiple myeloma [28], while some others have reached to clinical trials [25,29–32]. However, the clinical applicability of the hydroxamic acid-based HDAC inhibitors is hindered by toxicities and off-target effects, resulting from poor selectivity over other metalloenzymes as well as within HDAC family subtypes [33–35]. Other disadvantages of the hydroxamic acid moiety include potential mutagenicity [36,37] and susceptibility to metabolic inactivation, mainly via glucuronidation [38–40].

Consequently, the design and development of HDAC inhibitors bearing different ZBG other than hydroxamic acid have recently gained growing interest [41–43]. We recently reported the development of novel class I HDAC inhibitors bearing alkyl hydrazide moiety as ZBG with T cell modulatory properties [42]. In addition, an alkyl hydrazide HDAC3 inhibitor (LSQ-28) with oral bioavailability and anticancer properties was reported [44]. Furthermore, Stopper et al. described the development of an ethyl hydrazide compound (DS-103) as class I HDACs as well as HDAC6 inhibitor with chemo-sensitizing properties [45].

So far, only SIS17 has been reported as a selective inhibitor bearing alkyl hydrazide ZBG against HDAC11. In the current study, we report the development of a ligand-based virtual screening workflow utilizing a categorical classification model (Fig. 1) to identify new HDAC11 inhibitors bearing an alkyl hydrazide ZBG through screening of a designed specific chemical space. Of the identified potential HDAC11 inhibitors, two compounds were selected for further analysis and development. The compounds were synthesized and examined by in vitro enzymatic evaluation. Furthermore, the binding mode of the compounds was studied by molecular docking and verified by molecular dynamics simulation and metadynamics studies.

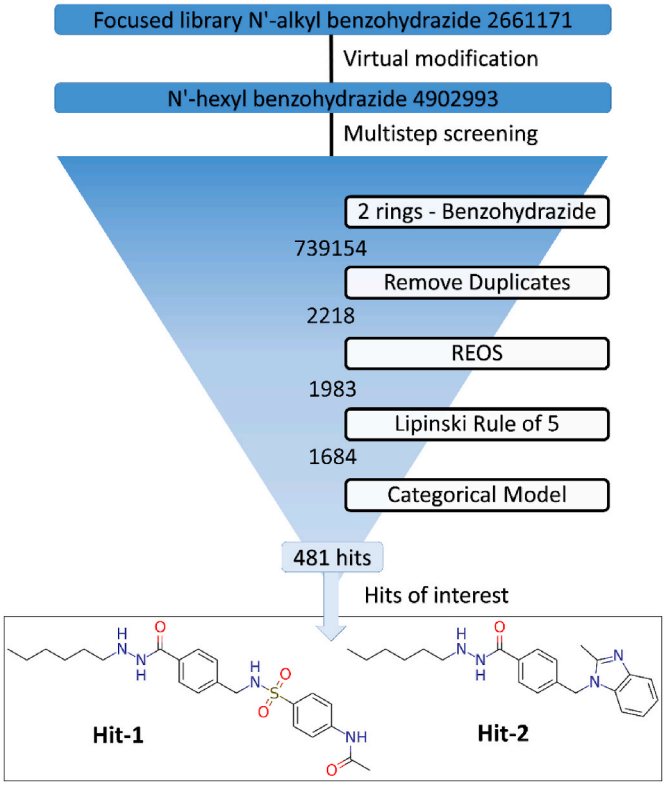

Fig. 1. Schematic representation of the virtual screening workflow.

2. Results and discussion

2.1. Virtual screening

2.1.1. Design of focused chemical space

Virtual screening employs computational methods to search large compounds databases for potential active compounds against certain targets. It offers a faster and more cost-effective way, compared to experimental methods, to identify new lead molecules, which can subsequently be optimized to meet the desired characteristics such as efficacy and safety [46–48]. ZINC20 is a publicly accessible database that contains nearly two billion compounds in 2D and 3D downloadable formats through an online platform that allows for rapid search for compounds [49]. While hydroxamates in general represent a well-established pharmacophore for HDAC inhibitors and are recognized as the most commonly utilized ZBG in HDAC inhibitors, benzohydroxamates represent a significant category of HDAC inhibitors, and their advancement involves an active area of research for the design of inhibitors for various HDAC subtypes [23]. For this reason and in order to identify new alkyl hydrazides as HDAC11 inhibitors, a focused library of N'-alkyl benzohydrazide compounds was obtained from the ZINC20 database by using a SMARTs pattern search. The acquired database was then virtually modified to create a specific chemical space. The virtual modification involved the replacement of the various N'-alkyl substitutions of the hydrazide moiety with an N'-hexyl group (Fig. 2). For optimal efficacy and selectivity towards HDAC11 inhibition, a substitution of 6-carbon long alkyl chain was selected based on previous results obtained from an in-house alkyl hydrazide inhibitors database.

2.1.2. Database filtering

Molecular filters are commonly used in virtual screening to narrow down the chemical space by removing compounds with chemical structures and properties that do not match the scope of interest. Most of such filters are primarily designed to define and extract drug-like and bioavailable molecules from large libraries [50]. Drug-likeness can be defined as a set of desired properties that are often observed in clinically approved drugs, such as water solubility, oral absorption, membrane permeability, suitable clearance rate and low toxicity [50–52]. After the virtual modification, the designed specific chemical space was subjected to multiple filtering procedures. The new database was first filtered to eliminate fragments with less than two rings and to select benzohydrazide compounds followed by the removal of duplicate structures, which resulted from the modification step.

To identify new HDAC11 inhibitors with drug-like properties, rapid elimination of swill (REOS) and Lipinski rule of five filters were then applied. REOS filter [46,50,53] is a structural filter that includes 117 SMARTS strings used to define substructures that are associated with nondrug-like molecules or possess known toxicity. This filter can eliminate compounds with known reactive groups that may induce multi-target binding and nonspecific interactions, leading to interference with biological assays [50,53]. The Lipinski rule of five is commonly used to identify bioavailable drug-like compounds. It was designed based on the analysis of 2245 compounds from the World Drug Index, which could identify molecular properties that are probably associated with orally available drugs [50,54]. For a compound to comply with the rule of five, it must meet the following criteria: molecular weight <500 Da, logP <5, H-bond donors <5, and H-bond acceptors <10 [54,55]. 1684 compounds successfully passed the REOS

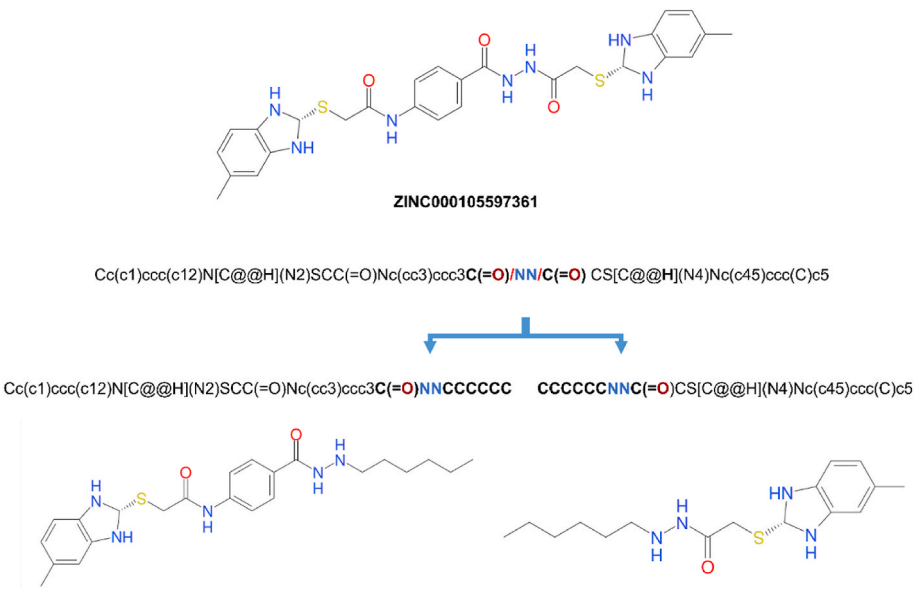

Fig. 2. Illustration of the virtual modification process to design a suitable specific chemical space for HDAC11 inhibitors.

and Lipinski rule of five filters.

2.1.3. Developing and utilizing the categorical classification model

2.1.3.1. Model development. The categorical model employed Bayes classification, which is a probabilistic approach based on Bayes' theorem [56]. In the context of drug design and discovery, Bayesian methods are used to identify the probability of a small molecule exhibiting biological activity towards certain target or enzyme [57,58]. For the developed model, a binary Bayes classifier was generated using a training set of instances where each instance is known to belong to one of two classes, active or inactive. Each instance in the training set is described by a single feature, namely, radial fingerprints. The classifier learns to distinguish between the classes by analyzing how often the feature appears in each class [59]. Radial fingerprints [60,61], also known as extended connectivity fingerprints (ECFPs) [62,63], is a type of topological 2D fingerprints, specifically designed for structure-activity modeling [63]. These fingerprints are generated by expanding fragments radially from each heavy atom. Each unique fragment is then converted into a distinct integer through hashing the description of the fragment's atoms and connectivity pattern [61,63]. The classification model was developed using 80 alkyl hydrazide HDAC11 inhibitors from our in-house database. The compounds were assigned either active (32 compounds) or inactive classes (48 compounds) as discussed in the **Materials and methods** section.

Several metrics are used to assess the performance of classification models [64,65]. Accuracy can provide a comprehensive evaluation of the performance of the model by determining the percentage of all correctly classified compounds. A more detailed insight into the performance of the model can then be gained through the confusion matrix, which provides a comparative representation of the model predictions against the assigned true labels [64].

In a confusion matrix, sensitivity refers to the ability of the model to identify the active compounds or positive instances and is expressed as the ratio of predicted true-positive instances to the total number of positive cases. Specificity is the ability of the model to correctly predict the inactive compounds or negative instances and can be represented as the ratio of true-negative instances to the total number of negative data points [64,65]. The developed classification model demonstrated excellent performance with accuracy, specificity and sensitivity exceeding 90 % (Table 1).

Table 1
Confusion matrix of the developed categorical model.

Categorical model					
Activity	Correct	Incorrect	Total		
0	45	3	48	**specificity**	**93.75**
1	31	1	32	**sensitivity**	**96.88**
Total	76	4	80	**accuracy**	**95.00**

2.1.3.2. Model validation. To validate the initially developed categorical model, the compounds from the in-house dataset were divided into training and test sets. To ensure homogenous distribution of the chemical scaffold and activity class when selecting the training and test sets for validation, the compounds in the dataset were first classified and arranged according to their scaffold subset. Additionally, within each subset, compounds were arranged based on their activity class. The selection of the training and test sets was then carried out using the procedure outlined in **Materials and methods section**, yielding four different training sets along with their corresponding test sets.

The external validation of the categorical model demonstrated a robust performance across the four different training and test sets (Table S5). The overall accuracy ranged between 80 % and 85 % for the four test sets, while the specificity was between 85 % and 92 %. Although the sensitivity showed a lower range of 71 % to 80 %, this might not impose a significant issue when searching large databases to identify active compounds.

2.1.3.3. Model application. Before using the model to classify the designed and filtered chemical space and to ensure the reliability of the predictions, the applicability domain (AD) of the model was computed and applied. AD can be determined based on the chemical similarity/dissimilarity indicated by similarity distances [66,67]. A large similarity distance suggests that a test compound is more dissimilar than can lie within the applicability domain of the training set.

To determine the AD of the model, Euclidian distances [66–68] were calculated using the same descriptor employed to develop the model, the radial fingerprints. The distance threshold/applicability domain was then calculated as detailed in the **Materials and methods section** and was applied to the designed compounds database. 1620 compounds were found to fall within the AD of the developed model. The categorical model was subsequently utilized to predict the class of these compounds,

and 481 compounds were predicted to be active.

Two compounds were considered to be of particular interest when searching for active and selective HDAC11 inhibitors because they share structural similarity to hydroxamic acid inhibitors, which have been reported to exhibit selectivity towards HDAC6 over other HDACs [69–74] (Fig. 3). The X-ray crystal structures of two of these hydroxamic acid analogues in complex with HDAC6 have been determined and reported, namely, PDB: 7UK2 [73] and 6ZW1 [72].

The absence of the foot pocket in class IIb HDACs and their inability to accommodate long alkyl chain attached to the ZBG, suggests that the replacement of the hydroxamic acid group by hexyl hydrazide will demolish the inhibitory activity towards HDAC6. Since the hit compounds from the virtual screening were predicted to be active inhibitors towards HDAC11 by the categorical model, this change might then offer a chance to develop inhibitors with absolute selectivity towards HDAC11. Similarly, in their study, Kozlov et al. [75] showed that converting the hydroxamic acid functionality of **hit-2** analogue (compound **32**) [74] to propyl hydrazide (Compound **12a-PH**) shifted the selectivity towards class I HDACs rather than HDAC6.

2.2. Chemistry

The two selected virtual screening hits were synthesized according to Scheme 1. For **hit-1**, the sulphonamide intermediate compound **3** was synthesized by coupling N-acetylsulfanilyl chloride **1** and methyl 4-(aminomethyl)benzoate **2** using diisopropylethylamine (DIPEA) as a base. For **hit-2**, the alkylation of 2-methylbenzimidazol **6** using methyl 4-(bromomethyl)benzoate **7** in presence of DIPEA afforded intermediate **8**. The ester derivatives **3** and **8** were then condensed with hydrazine hydrate to afford the acid hydrazide intermediates **4** and **9**, which were further subjected to reductive amination using hexanal to afford the alkyl hydrazide hits **5** (**hit-1**) and **10 (hit-2)**.

2.3. In vitro enzymatic evaluation

The two hit compounds were evaluated by in vitro enzymatic testing and both demonstrated potent inhibition of HDAC11 with IC_{50} of 172.19 ± 18.45 nM and 21.98 ± 1.85 nM for **hit-1** and **hit-2**, respectively. In order to assess the selectivity of the identified hits, the compounds were screened for the inhibition of all other isoforms from class I and class II HDACs. Both compounds could demonstrate selective inhibition of HDAC11 at 1 μM concentration except for HDAC8, for which a considerable inhibition was also observed (Table 2 and Fig. 4).

The IC_{50} values of **hit-1** and **hit-2** for HDAC8 were profiled and found to be 14.86 ± 1.0 nM and 14.09 ± 0.4 nM, respectively. We also included the alkyl hydrazide inhibitor SIS17 as a reference in our enzymatic assays and it measured 170 ± 10 nM IC_{50} for HDAC11. The ability of the identified hits to inhibit the enzymatic activity of both HDAC11 and HDAC8 with high potency may be understood in the light of possessing similar structural features. The folding of loop-3 in both isoforms allows for the formation of a foot pocket [18,76] which can accommodate longer alkyl chains as reported by studies identifying both HDAC isoforms to possess defatty-acylase activity [18,19,77].

These findings show that the strategy we employed through the ligand-based virtual screening of a specific chemical space was successful in identifying potent HDAC11 inhibitors. While the selectivity of the compounds towards HDAC11 needs to be enhanced, these identified inhibitors can still be considered promising lead compounds as a starting point for lead optimization process, which is a common practice subsequent to lead identification by virtual screening.

2.4. Molecular docking studies

As members of the metal dependent HDACs family, HDAC11 and HDAC8 depend on the zinc ion for their catalytic activity. Analysing the active site reveals that the zinc ion is located at the depth of a funnel shaped binding site that is lined by seven loops. The zinc ion is coordinated by residues Asp181/178, His183/180 and Asp261/267 (HDAC11/HDAC8). Three main residues were identified to be essential for the catalytic activity of HDACs besides the zinc ion, a tandem histidine residues in loop-3 and a catalytic tyrosine residue in loop-7 (His142, His143 and Tyr304/306 for HDAC11/HDAC8).

A proposed catalytic mechanism for the metal-dependent HDACs involves the tandem histidine residues His142 and His143 functioning as a general base and general acid, respectively. In this mechanism, His142 acts as the general base by deprotonating the metal-coordinated water molecule, thereby activating it for nucleophilic attack on the substrate's carbonyl group. The resulting oxyanion is stabilized by the zinc ion and a hydrogen bond from Tyr304/306 (HDAC11/HDAC8). Meanwhile, His143 is thought to serve as the general acid, donating a proton to the departing amine group, which promotes the breakdown of the intermediate into the final products, lysine and acetate [78,79]. An alternative mechanism suggests that His143 acts alone as both the general base and general acid during catalysis, while His142 remains

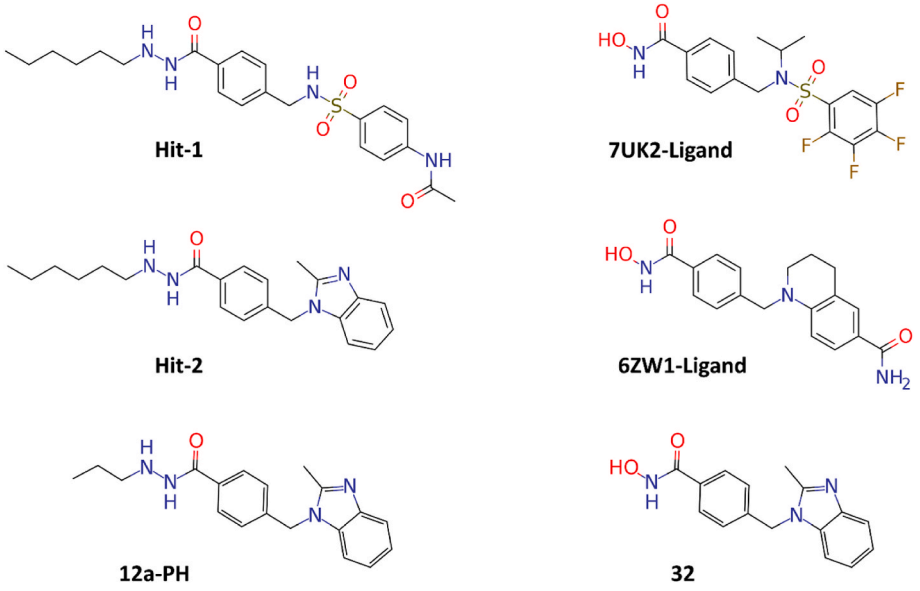

Fig. 3. 2D structures of the two identified hits and structurally related inhibitors from literature.

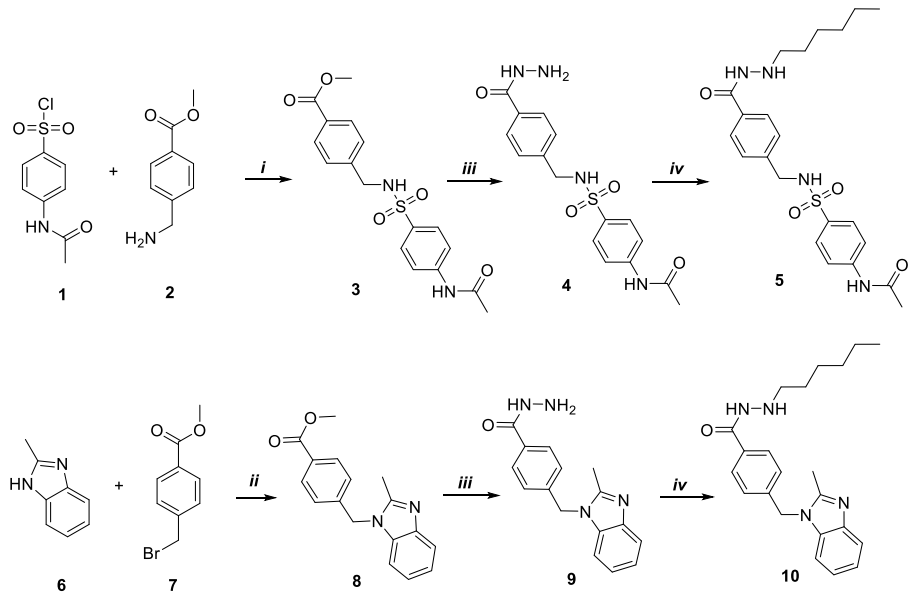

Scheme 1. Synthesis of target compounds. Reagents and conditions: (i) DIPEA/DCM/RT/1h; (ii) DIPEA/DCM/50 °C/overnight; (iii) $N_2H_4.H_2O$/ethanol/reflux/2h; (iv) Hexanal/pTSA/methanol/RT/1h then $NaBH_4$/4h.

Table 2
Percent inhibition values of **hit-1**, **hit-2** and SIS17 at 1 μM concentration against HDAC isoforms.

	Hit-1		Hit-2		SIS17	
	% inhibition	SD[a]	% inhibition	SD[a]	% inhibition	SD[a]
HDAC1	20.2	4.8	40.7	2.2	0	1.5
HDAC2	6.9	3.7	34.6	0.6	3.8	3.1
HDAC3	9.0	1.3	8.4	0.8	0	3.7
HDAC4	18.9	4.6	12.9	2.1	0	2.9
HDAC5	3.4	5.0	2.4	1.6	0	1.2
HDAC6	7.1	1.8	4.6	2.3	0	1.9
HDAC7	8.2	4.6	10.7	3.8	0	0.9
HDAC8	97.8	1.7	97.3	1.4	4.4	3.0
HDAC9	10.2	0.9	17.0	1.0	0.1	5.9
HDAC10	12.4	1.8	1.4	2.8	2.2	2.8
HDAC11	86.8	1.2	99.3	1.0	72.2	0.3

[a] Standard deviation, all tests were done in three replicates.

protonated and act as electrostatic catalyst to stabilize the transition state [78].

Notably, the H142A mutant of HDAC8 exhibited a 230-fold reduction in enzymatic activity compared to the wild type. In comparison, the H143A and H142A/H143A mutations led to an even more dramatic loss of activity by more than 8000-fold. Moreover, the Y306F HDAC8 mutant reduced the enzymatic activity by 150 folds [78]. These findings highlight the critical roles of these residues, besides the zinc ion, for the catalytic activity of HDACs and underscore the importance of considering them when designing ZBG for HDACs inhibitors.

Previously, we reported the optimization of HDAC11 AlphaFold2 model and its utilization to study the binding mode of the alkyl hydrazide SIS17 [76]. In the current study, we utilized this optimized model for the molecular docking of the selected hits. In the obtained docking poses, both compounds demonstrated a bidentate chelation of the zinc ion through the carbonyl oxygen and the nitrogen of the alkyl hydrazide group with distances ranging between 2.35 Å and 2.42 Å. Three hydrogen bonds were observed between the carbonyl oxygen and the two NH atoms of the hydrazide moiety and Tyr304, His142 and His143, respectively (Fig. 5A and B). The alkyl chain of the ligands occupied the foot pocket and could form hydrophobic interactions with residues Phe37, Phe141, Phe152 and Cys153. The 2-methylbenzimidazole and the acetanilide capping groups exhibited a bent conformation oriented towards loop-1 and loop-2 and formed hydrophobic interactions with Pro36. Furthermore, for **hit-1**, an additional hydrogen bond was observed between the NH of the acetanilide capping group and the backbone carbonyl oxygen of Glu94. Interestingly, the predicted binding mode of the selected compounds in HDAC11-AF2 model demonstrated

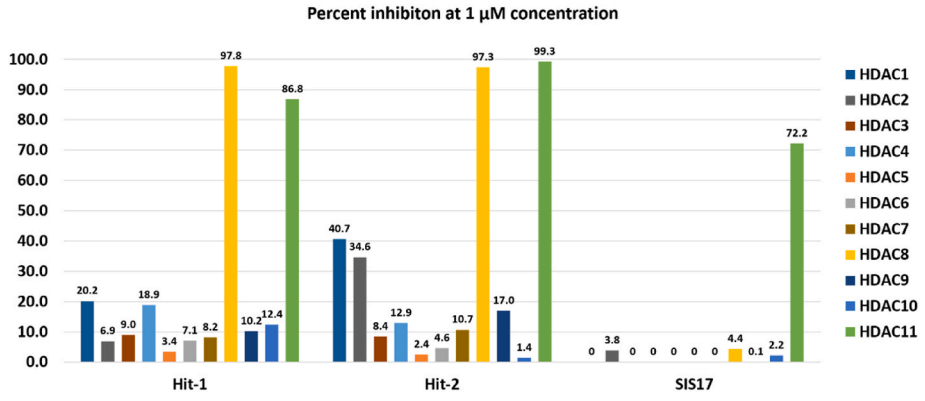

Fig. 4. Primary screening of the two identified hits and reference inhibitor SIS17 against HDAC subtypes (% of inhibition at 1 μM concentration).

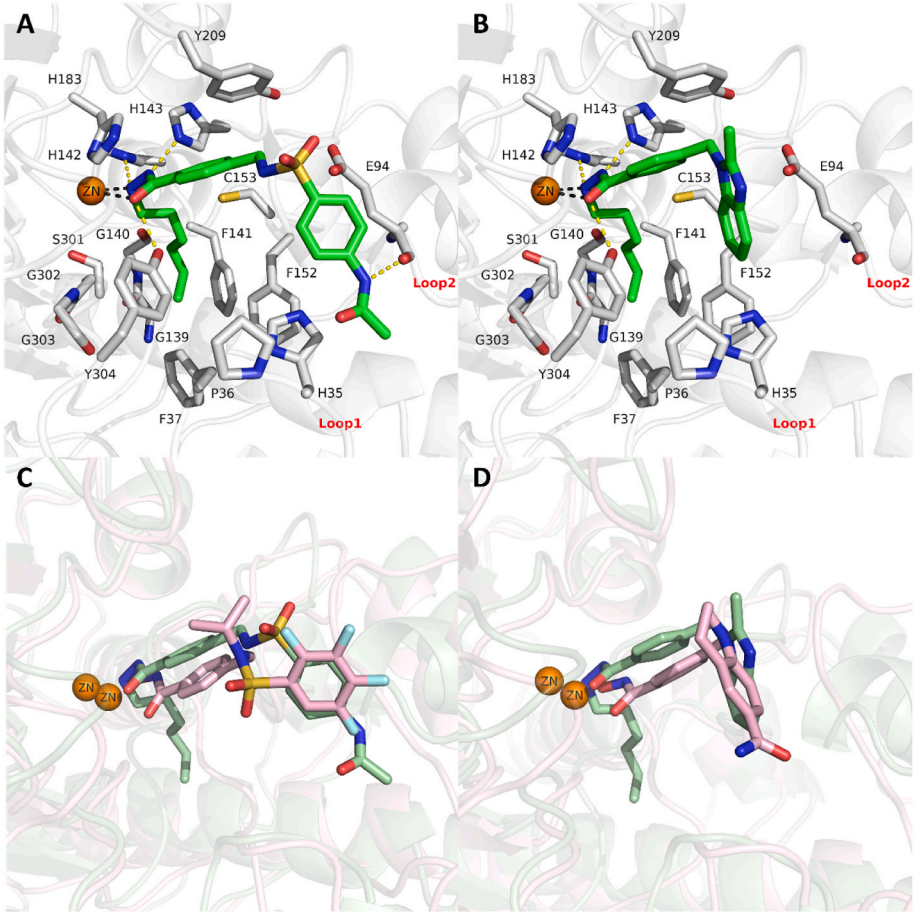

Fig. 5. (**A**) and (**B**). The docking poses of the first and second virtual screening hits, respectively, in HDAC11. The protein backbone appears as white cartoon, interacting residues of the binding site as grey sticks, zinc cofactor as orange sphere and ligands as green sticks. Hydrogen bonds are represented as yellow dashed lines and coordination bonds as grey dashed lines. (**C**) and (**D**). Superposition of the docking poses of the first and second virtual screening hits in HDAC11 (pale green) with similar hydroxamic acid analogues from HDAC6 crystal structures (light pink) PDB: 7UK2 and 6ZW1, respectively. (For interpretation of the references to colour in this figure legend, the reader is referred to the Web version of this article.)

an orientation that is similar to their hydroxamic acid analogues co-crystallized with HDAC6 (Fig. 5C and D).

The binding mode of the identified compounds in HDAC8 was also studied by molecular docking. For both compounds, the docking poses (Fig. 6) demonstrated that the carbonyl oxygen and one nitrogen of the hydrazide moiety coordinated the zinc ion in a bidentate fashion with distances ranging between 2.21 Å and 2.32 Å. The hydrazide group formed three hydrogen bonds with residues His142, His143 and Tyr306.

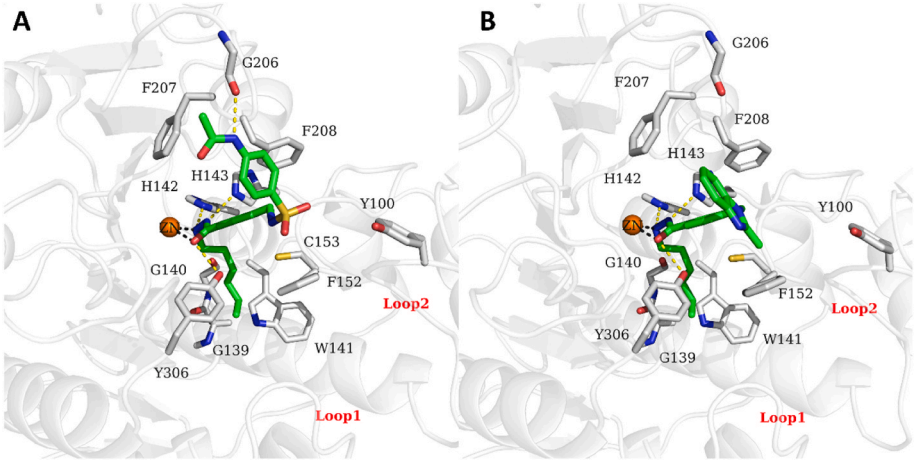

Fig. 6. (**A**) and (**B**). The docking poses of the first and second virtual screening hits, respectively, in HDAC8. The protein backbone appears as white cartoon, interacting residues of the binding site as grey sticks, zinc cofactor as orange sphere and ligands as green sticks. Hydrogen bonds are represented as yellow dashed lines and coordination bonds as grey dashed lines. (For interpretation of the references to colour in this figure legend, the reader is referred to the Web version of this article.)

The hexyl chain is accommodated in the foot pocket and formed hydrophobic interactions with Trp141 and Cys153. Although, the hydrazide group and the alkyl chain of the compounds in HDAC8 showed interactions and orientation similar to what was observed in HDAC11, the docking poses of the two compounds in HDAC8 showed different orientation of the capping group compared to their predicted binding mode in HDAC11. For **hit-1**, the capping group was directed towards loop-5 allowing for the formation of an additional hydrogen bond between the NH of the terminal acetanilide and the carbonyl oxygen of Gly206. While for **hit-2**, the 2-methylbenzimidazole group flipped for better accommodation between loop-5 and loop-6. It is worth noting that different orientations of the capping group of quisinostat were observed before in two different HDAC8 crystal structures, namely 6HSK which is a crystal structure of a human HDAC8 loop-6 mutant and 6HSH that is a crystal structure of Schistosoma mansoni HDAC8 [80].

2.5. Molecular dynamics simulation studies

The docking poses of the virtual screening hits of interest in HDAC11 were then subjected to molecular dynamics (MD) simulation to gain a deeper insight regarding the predicted binding mode. The RMSD plots from the short (50 ns) (Figs. S2 and S4) MD simulations for both hit compounds demonstrate that the protein is stabilizing between 1 and 2 Å while the zinc ion is stabilizing below 1 Å indicating for the high stability of the system over the course of simulation. The ligand RMSD of **hit-1** (Fig. 7A) exhibited a shift during the simulation and stabilized at around 3 Å. Inspecting the RMSF plots (Fig. 7B), showed that the capping group is the most fluctuating substructure of the ligand while all the other ligand heavy atoms are fluctuating below 2 Å. Moreover, the MD trajectories were analyzed to further investigate the observed fluctuations. The analysis revealed that the sulfonamide group adopts an opposite conformation during the simulation compared to the starting docking pose (Fig. S3).

The new conformation brings the oxygen atoms of the sulfonamide group closer to loop-1, thus making them available for hydrogen bond formation with His35 and the fluctuating catalytic Tyr304. The fluctuation of the Tyr304 side chain [76] led to the complete loss of the hydrogen bond with the carbonyl oxygen of the hydrazide group that was initially observed in the docking pose. Additionally, during the simulation, a hydrogen bond was formed between the NH of the sulfonamide group and Glu94 side chain, either directly or through a water bridge, while the hydrogen bond between the NH of the terminal amide group and the backbone carbonyl oxygen of Glu94 was almost completely lost.

The hydrogen bond stability during the simulation was monitored (Table S1, Figs. S6 and S8) and revealed a very high stability for His142 and His143 with persistence ranging between 97 % and 100 %. The hydrogen bond formed during the simulation between the oxygen of the sulfonamide group and Tyr304 showed intermediate to high stability with persistence percent of 55 % and 94 % for two independent MD simulations. The newly formed hydrogen bonds with His35 and Glu94 demonstrated intermediate stability that ranged between 39 % and 51 %.

The long (500 ns) MD simulation of **hit-1** showed similar RMSD pattern for the protein backbone, the zinc ion and the ligand (Fig. 8A). Additionally, the RMSF plot (Fig. 8B) of the ligand heavy atoms and the inspection of the MD trajectories (Fig. 9) confirmed the fluctuation of the capping group and the stabilization of the opposite conformation as observed in the short MD simulations. The hydrogen bonds with His142 and His143 showed high stability with persistence above 99 %, while the newly formed hydrogen bond between the oxygen of the sulfonamide group and Tyr304 demonstrated a persistence of about 83 %. The

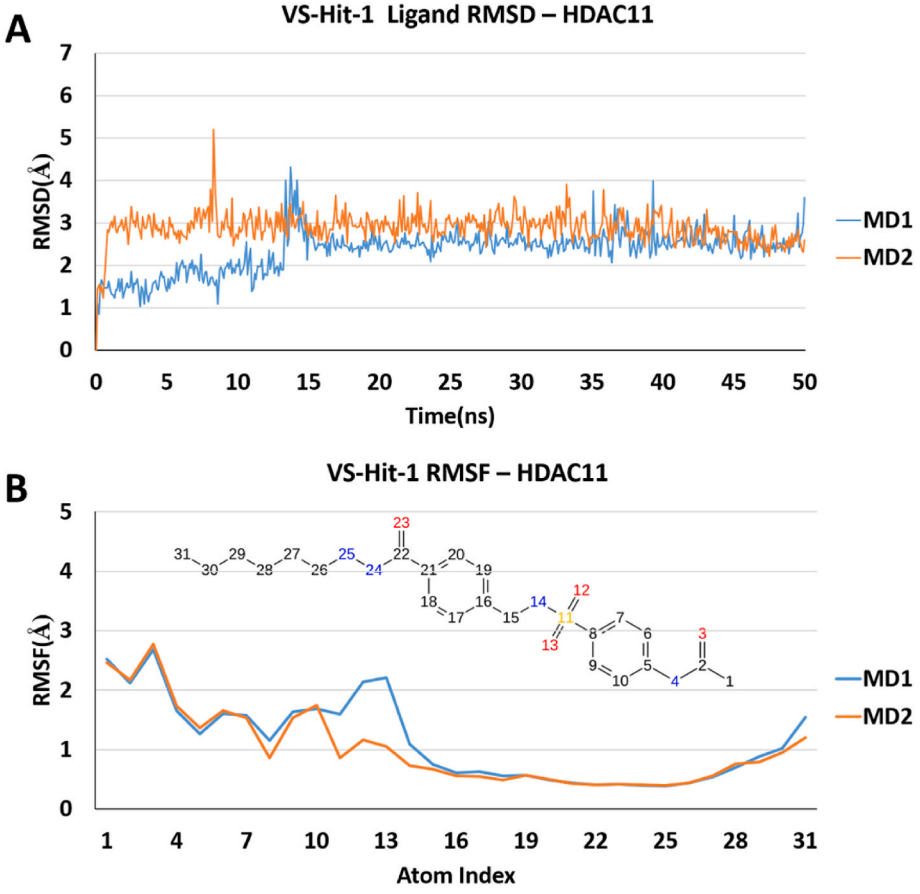

Fig. 7. (**A**) and (**B**). RMSD and RMSF plots, respectively, of ligand heavy atoms of **hit-1** in HDAC11 for two 50 ns independent MD simulations.

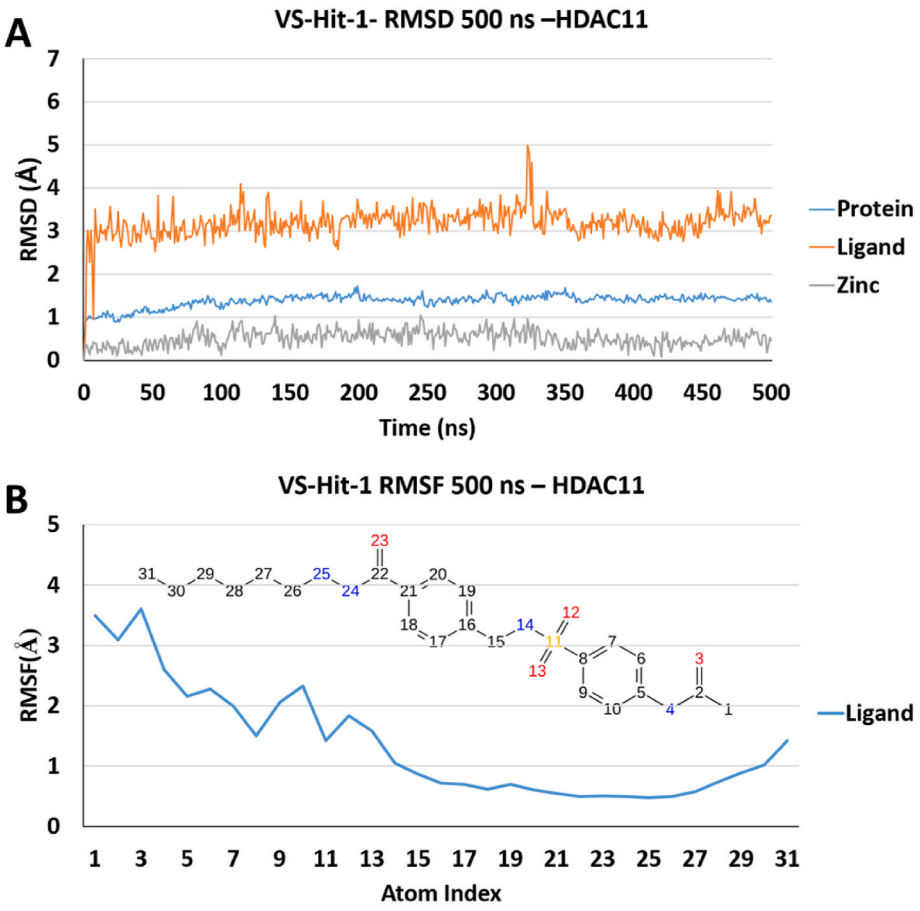

Fig. 8. (**A**). RMSD plots of the protein backbone, the ligand heavy atoms and the zinc ion of **hit-1** in HDAC11 from the long (500 ns) MD simulation. (**B**). RMSF plot of the ligand heavy atoms of **hit-1** in HDAC11 from the long (500 ns) MD simulation.

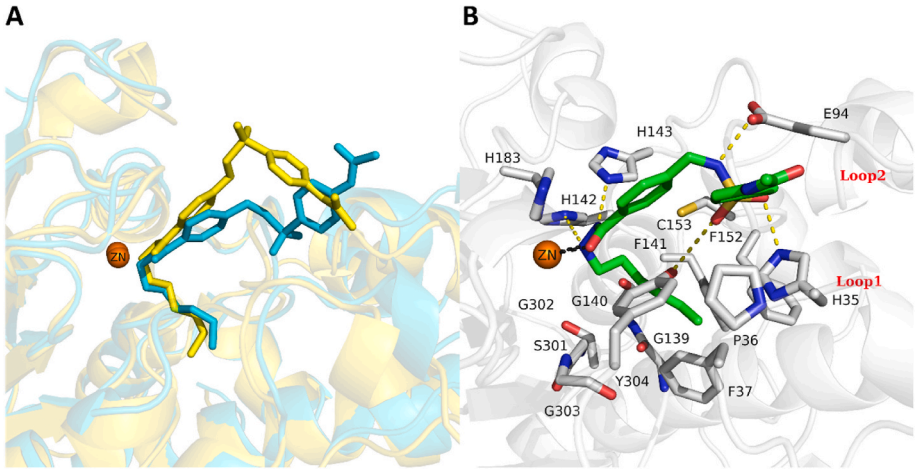

Fig. 9. (**A**). Superposition of the first (yellow) and last (cyan) frames of **hit-1** in HDAC11 from the long (500 ns) MD simulation demonstrating the shift of the ligand pose. The zinc ion is represented as an orange sphere, the protein backbone as cartoon and the ligand as sticks. (**B**). Selected frame from the long (500 ns) MD simulation of **hit-1** in HDAC11 demonstrating the newly established interactions during the simulation. The protein backbone appears as white cartoon, interacting residues of the binding site as grey sticks, zinc cofactor as orange sphere and ligand as green sticks. Hydrogen bonds are represented as yellow dashed lines and coordination bonds as grey dashed lines. (For interpretation of the references to colour in this figure legend, the reader is referred to the Web version of this article.)

stability of the hydrogen bonds with His35 and Glu94 was lower than average with persistence around 32 % (Table S1, Figs. S10A and S11A).

To further investigate the change in the pose of **hit-1** during the MD simulation we applied metadynamics, which is an enhanced sampling technique that can explore structural dynamics more efficiently within a limited time scale. This is achieved by applying a history-dependent bias potential as a function of a selected collective variable, allowing the system to escape local minima and avoid revisiting already sampled regions, thus accelerating the sampling of the entire free-energy landscape of the protein-ligand complex [81].

We applied the binding pose metadynamics (BPMD) [82] implemented in Schrödinger modelling suite. It was originally developed to

differentiate between and rank different docking poses of a single ligand in a single protein binding site by running a series of metadynamics simulations and using the RMSD of the ligand as a collective variable. We applied BPMD to the initial docking pose and the stabilized pose from the last frame (500 ns) of the classical MD simulation of **hit-1** to examine the significance of the change in ligand pose in the classical MD simulation.

The results from the BPMD can give a figure about the stability of the protein-ligand complex through monitoring the ligand's RMSD fluctuations and the persistence of initial interactions between the ligand and the receptor during simulation. The PoseScore represents the average RMSD of the ligand, the PersScore represents the average persistence of the initial interactions over the course of simulation, while the CompScore combines both PoseScore and PersScore [82,83].

The results for **hit-1** demonstrated a PoseScore of 3.184 and 1.168 for the initial docking pose and the pose from the last MD frame, respectively (Fig. 10). In general, PoseScore that is $\leq$ 2 Å indicates for a stable pose [82]. The interaction persistence of the last frame pose was significantly higher with a PersScore of 0.941 compared to a PersScore of 0.484 for the initial docking pose. This is also in agreement with a previously defined threshold of $\geq$0.6 to indicate for a well maintained protein-ligand interactions network [82]. The CompScore for the starting docking pose and the pose from the last MD simulation frame of **hit-1** were found to be 0.763 and −3.536, respectively, with increasingly negative values reflecting higher stability.

The results from the BPMD indicate that the equilibrated pose of **hit-1** during the classical MD simulation is more stable when compared to the starting docking pose, thus supporting the results obtained from the classical MD simulation.

In the short MD simulations, the RMSD plots (Fig. 11A) of **hit-2** demonstrate high stability of the ligand, which is stabilizing below 2 Å, while almost all the ligand heavy atoms are fluctuating below 1 Å as observed in the RMSF plots (Figs. 11B and S5). The hydrogen bond stability for His142 and His143 were very high with persistence ranging between 98 % and 100 %, while for Tyr304 the hydrogen bond was almost completely lost (Table S2, Figs. S7 and S9) due to the fluctuation of the side chain of this residue.

The long MD simulation of **hit-2** also confirmed the stability of the ligand as reflected in the RMSD and RMSF plots (Figs. 12A and B and S12) as well as the stability of the hydrogen bonds with His142 and His143 with persistence of about 99 % and 98 %, respectively (Table S2, Figs. S10B and S11B).

The docking poses of the identified hits in HDAC8 were also studied by MD simulation. The RMSD plots for both hits showed that the protein backbone and the zinc ion are stabilizing between 1 and 2 Å (Figs. S13 and S15). For **hit-1**, the RMSD (Fig. 13A) of the ligand showed a high shift directly after the simulation started and stabilized at around 7 Å. Inspecting the MD trajectories, revealed that the capping group shifted to an opposite conformation, thus directed towards loop-2 rather than loop-5 that was observed in the starting docking pose (Fig. S14). This observation is also in agreement with the RMSF (Fig. 13B) of the ligand in which the heavy atoms of the capping group are showing the highest fluctuation. This shift in the pose lead to complete loss of the initially observed hydrogen bond between the terminal NH of the capping group and Gly206 in loop-5 and allowed for the formation of another hydrogen bond between the same NH and Tyr100 in loop-2. The hydrogen bond persistence (Table S3, Figs. S17 and S19) with His142 showed high stability above 99 %, while for His143; average stability between 53 % and 77 % was observed for two independent simulations. The newly formed hydrogen bond with Tyr100 showed also average stability between 43 % and 61 % for two independent MD runs.

The long MD simulation of **hit-1** in HDAC8 confirmed the results from the short MD runs in terms of RMSD and RMSF (Fig. 14) which are reflecting the shift of the ligand pose from the initial docking pose (Fig. S23A). The hydrogen bond with His142 showed to be highly stable with persistence above 99 %, while for His143 and Tyr100, average stability of 59 % and 44 %, respectively, was observed (Table S3, Figs. S21A and S22A).

We also examined the stability of the starting docking pose and the stabilized pose of **hit-1** in HDAC8 using BPMD (Fig. 15). The resulting PoseScores were 4.401 for the docking pose and 2.610 for the pose from the last MD frame, while the PersScores were found to be 0.350 and 0.714 for the docking pose and the equilibrated pose, respectively. These scores reflect the higher stability of the stabilized pose during the MD simulation compared to the initial docking pose. Additionally, The CompScores also confirmed these results with values of 2.651 and −0.958 for the docking pose and the last frame pose, respectively. Overall, the results from the BPMD supports the findings from the classical MD simulations.

For **hit-2**, the RMSD (Fig. 16A) of the ligand showed sharp fluctuations at the beginning of the simulation and stabilized at around 2 Å after about 25 ns (Fig. S16). Inspecting the RMSF plots (Fig. 16B) revealed that the capping group, specifically the phenyl ring of the 2-methylbenzimidazole showed the highest fluctuation during the simulation. The hydrogen bond with His142 showed very high stability with persistence around 100 %, while for His143 the stability was above average with persistence around 61 % (Table S4, Figs. S18 and S20).

For the long MD simulation, the hydrogen bonds with His142 and His143 showed high stability with persistence of 99 and 87 %, respectively (Table S4, Figs. S21B and S22B). The RMSD and the RMSF plots (Fig. 17), however did not confirm the stabilization of the capping group. As observed in the RMSD plots, the RMSD of the ligand showed sharp fluctuations reaching up to 4 Å over the course of the simulation. Examining the RMSF plots also showed higher fluctuation of the heavy atoms of the capping group (Fig. S23B).

When comparing the results from the MD studies in HDAC8 and HDAC11, it appears that the hydrogen bond with His143 shows less stability, for both compounds, in HDAC8 than in HDAC11, however we

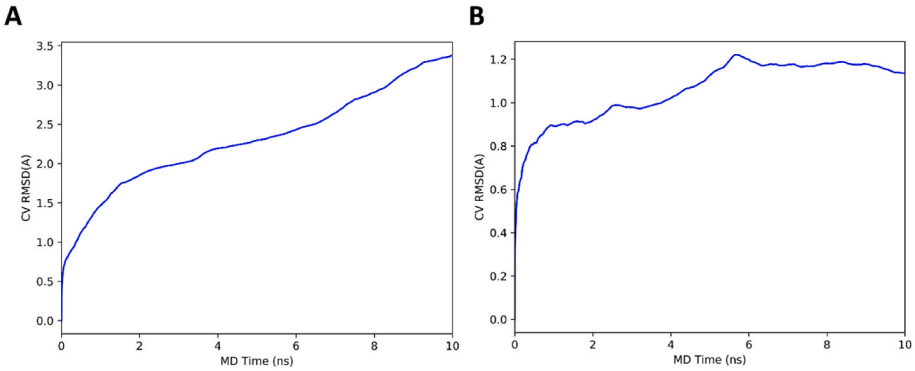

Fig. 10. Plots of the average collective variable (RMSD) over the BPMD simulation. (**A**) and (**B**). The starting docking pose and the shifted pose from last frame of the 500 ns MD simulation of **hit-1** in HDAC11, respectively.

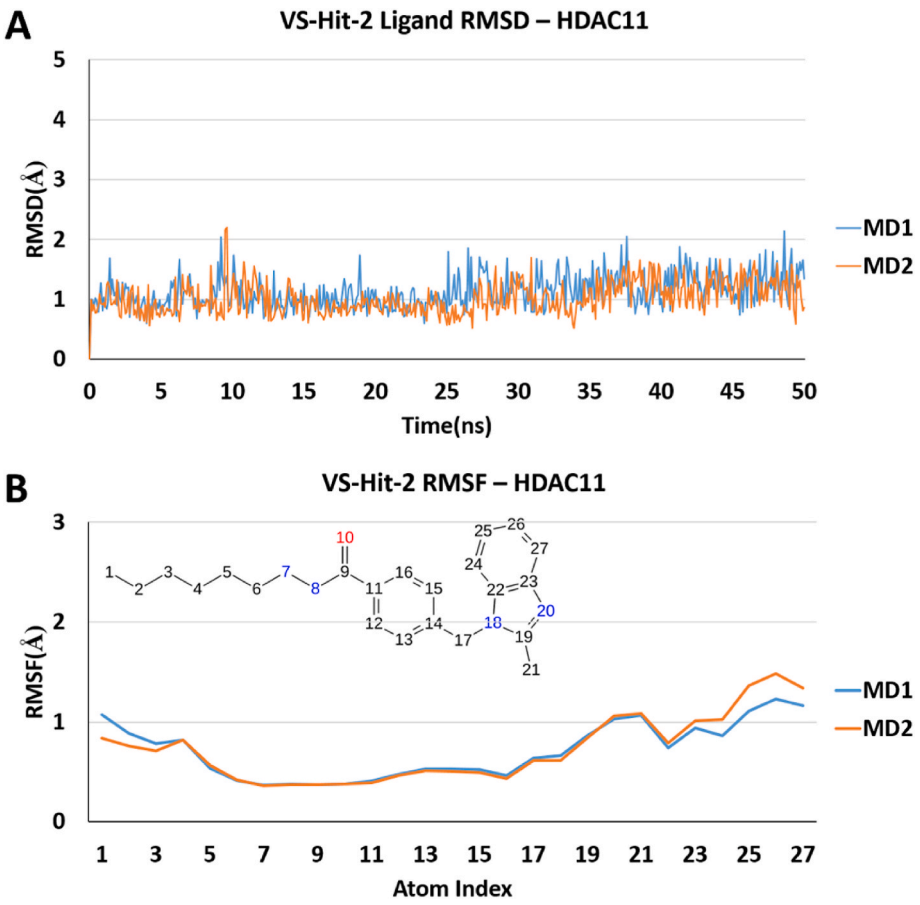

Fig. 11. (**A**) and (**B**). RMSD and RMSF plots, respectively, of ligand heavy atoms of **hit-2** in HDAC11 for two 50 ns independent MD simulations.

observed similar fluctuating behavior of this hydrogen bond in previous studies [17,76]. The less stability of the capping group of **hit-2** observed during the MD simulation in HDAC8 compared to HDAC11 can be understood in the light of the structural differences between the two isoforms, most importantly, the longer loop-1 in HDAC11. The length of this loop in HDAC11 allows for better shielding of the binding site (Fig. 18) making the capping group of the ligand less exposed to the solvent, thus conferring better stabilization to the capping group.

3. Materials and methods

Schrodinger Suite 2019 was used for all the modeling work, with Maestro interface [84] for visualization.

3.1. Protein structure and ligand preparation

HDAC8 crystal structure 5FCW was preprocessed using Protein Preparation Wizard [85,86]. Hydrogens were added and bond orders were assigned. Zero order bonds to metals were created and water 5 Å away from the ligands was deleted. Ionization states of the ligands were generated using Epik [87–89] at pH 7.0 ± 2.0. Waters with less than three hydrogen bonds with non-waters were removed. Hydrogen bond optimization was assigned automatically using PROPKA at pH 7.0.

The LigPrep [90] panel was utilized to prepare the ligands without changing the ionization states or generating tautomers or isomers.

3.2. Receptor grid generation

The Receptor Grid Generation panel was used to generate the receptor grid. For HDAC11, the vertical pose of SIS17 in the optimized HDAC11-AF2 model [76] was employed as the input protein-ligand complex. The centroid of the ligand was selected as the center of the grid box. All settings were kept as default, while ligand size was set to ≤ 25 Å to account for difference in ligand size.

Since there are no HDAC8 crystal structures cocrystallized with alkyl hydrazide inhibitors, HDAC8 crystal structure 5FCW was optimized by minimization in presence of N'-hexyl benzohydrazide fragment after the removal of the original cocrystallized ligand. For this, HDAC8 crystal structure and HDAC11 in complex with **hit-1** were aligned using the Protein Structure Alignment panel, then the coordinates of the alkyl hydrazide fragment were copied and merged with HDAC8 crystal structure. The merged structure was then minimized using Minimization panel from Desmond for 100 ps. The merged fragment was employed as the center of the grid Box, while the size of ligands to dock was increased to ≤ 30 Å to account for the difference in the ligand length.

3.3. Docking

Ligands docking was performed using Glide [91–94] and utilizing OPLS3e force fields [95–98]. SIS17 in HDAC11 and the alkyl hydrazide fragment in HDAC8 were selected as a core containing molecule for the restricted docking by using reference position. The core atoms were defined by maximum common substructure. The standard precision docking and flexible ligand sampling settings were employed. The top-scored poses were selected for further analysis.

3.4. Molecular dynamics simulation

The docking poses of the hit compounds were subjected to MD simulation using Desmond [99,100] and employing OPLS2005 force fields. Each pose was simulated for two independent short (50 ns) runs and a single long MD simulation of 500ns. The Protein Preparation Panel

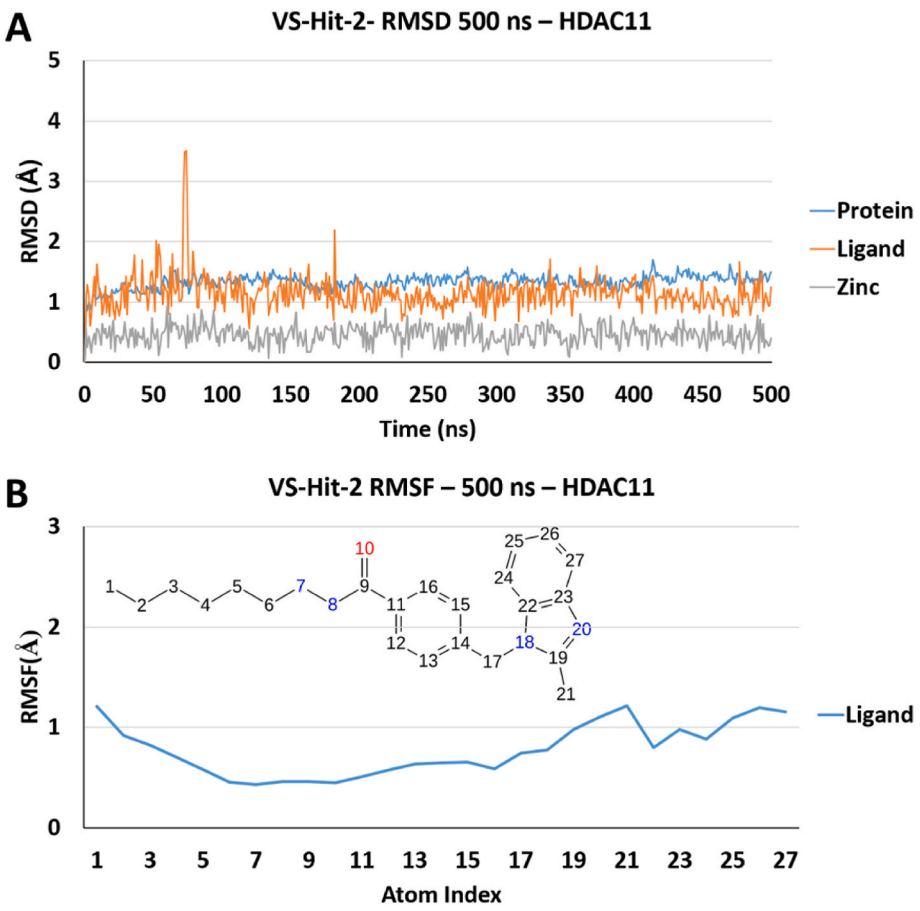

Fig. 12. (**A**). RMSD plots of the protein backbone, the ligand heavy atoms and the zinc ion of **hit-2** in HDAC11 from the long (500 ns) MD simulation. (**B**). RMSF plot of the ligand heavy atoms of **hit-2** in HDAC11 from the long (500 ns) MD simulation.

was used to create zero order bonds to the metal before submitting the protein ligand-complex to system preparation. The system was solvated in SPC water model using an orthorhombic box with 10 Å buffer distance. To neutralize the system, chloride or sodium ions were added 4 Å away from the ligand. The default Desmond relaxation protocol for NPT ensemble was used to relax the prepared system. A production run then followed the relaxation step and employed the NPT ensemble at temperature of 300 K using a Nose–Hoover chain thermostat and pressure of 1.01325 bar using Martyna-Tobias-Klein barostat. The progress of the simulation was recorded every 100 ps.

For analysis, the Simulation Event Analysis panel was used for RMSD calculations. The RMSD of the protein was calculated using the backbone atoms. For HDAC11 the termini (residues: 1–14 and 321–347) were excluded. To calculate the RMSD of the ligands and the zinc ion, fitting to the protein backbone was performed. The Simulation Interaction Diagram panel was used for analyzing the RMSF and the interaction persistence of the ligands.

Binding Pose Metadynamics panel was utilized to further investigate the shift in the pose of **hit-1**. The default settings of 10 simulations per pose each of 10 ns were kept. The original docked pose and the equilibrated pose (last frame) from the 500 ns MD run were used as input.

3.5. Properties calculations

The rule of five property was calculated using QikProp [101] properties from the Molecular Descriptor panel.

3.6. Categorical classification model

3.6.1. Building the categorical model

The categorical model was built using the Bayes classification application in Canvas [61,102,103] and utilizing radial fingerprints as descriptors. Radial fingerprints were generated using Binary Fingerprints from Structures panel in Canvas.

To train the model, an in-house dataset of 80 alkyl hydrazide compounds bearing different scaffolds was used. The dataset was classified into active and inactive categories using an IC_{50} value of 0.5 μM as a threshold.

3.6.2. Validating the categorical model

To validate the model, different training and test sets were created from the dataset. To ensure the homogeneity of distribution of the compounds between the training and test sets, the compounds in the dataset were arranged based on their chemical scaffold. Furthermore, compounds within each scaffold subset were arranged according to their activity class. The training and test sets were created by selecting every fourth entry as a test compound. This process was repeated four times starting from a different entry each time (starting from entry 1 to entry 4) and resulted in four different training and their corresponding test sets.

3.6.3. Applicability domain calculation

Euclidian distances were calculated for the compounds using the Similarity/Distance Matrix from Fingerprints panel in Canvas and employing the generated radial fingerprints. The average of all the distances was then calculated and distances below this average were

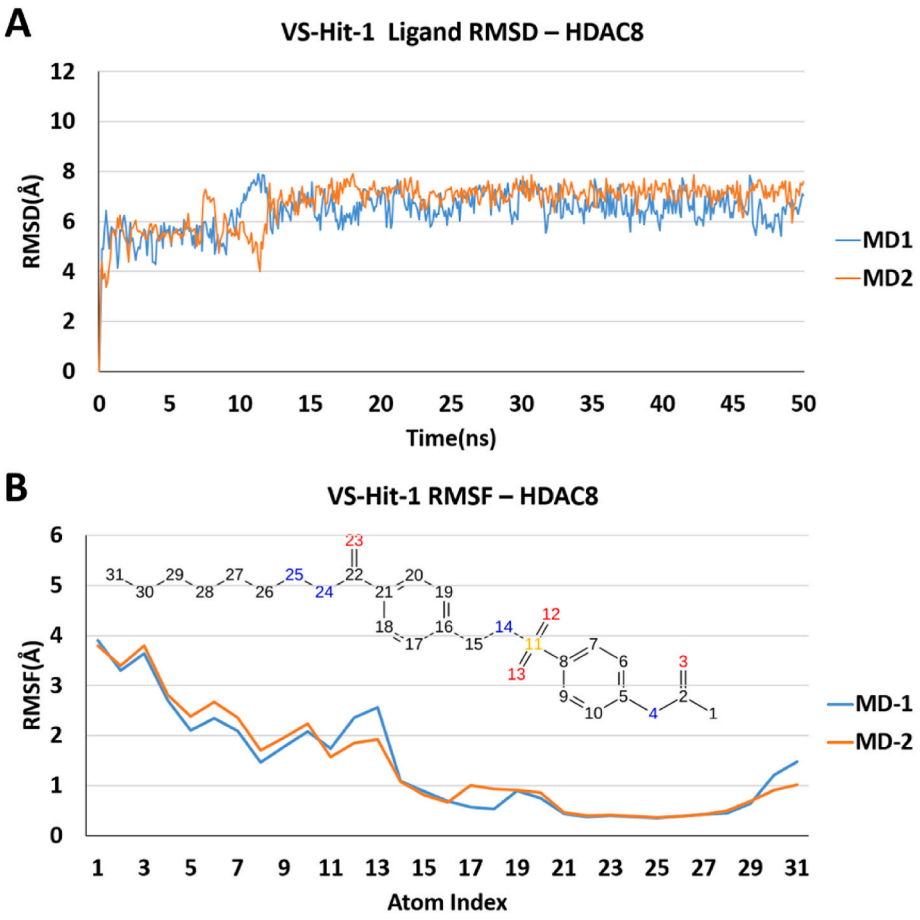

Fig. 13. (**A**) and (**B**). RMSD and RMSF plots, respectively, of ligand heavy atoms of **hit-1** in HDAC8 for two 50 ns independent MD simulations.

further used to calculate the new distance average term **Av** and the standard deviation term **σ** [104]. The applicability domain or distance threshold for the categorical model was then calculated using the following equation in which **Z** is an empirical parameter and the default value of 0.5 was used in this work [104,105]:

Applicability domain = Zσ +Av

3.7. Virtual screening

3.7.1. Dataset acquisition

A focused library of N'-alkyl benzohydrazide ligands (substructure SMILES: CN([H])N([H])C(=O)c1ccccc1) was downloaded from the ZINC20-all database [49] using the Arthor tool in the TLDR interface (tldr.docking.org) [106].

3.7.2. Virtual modification

The structures in the obtained library were modified virtually by converting the various N'-alkyl substitutions of the hydrazide moiety in the SMILES file to N'-hexyl group.

3.7.3. Multistep screening

The modified library was first filtered to remove fragments with less than 2 rings and to select benzohydrazide structures using Ligand Filtering panel followed by removing duplicate structures using the Merge Duplicates panel and Filter Duplicate function in Maestro. The cleaned library was then subjected to rapid elimination of swill (REOS) filter using the Structure Filter panel in Canvas. This step aimed to remove compounds bearing reactive or toxic groups that may interfere with biological assays. Compounds violating one or more property thresholds defined by the rule of five were eliminated from the library by using Ligand Filtering panel and the calculated rule of five property. Finally, the categorical model was employed to classify the filtered dataset to active and inactive compounds subsequent to an applicability domain filtration.

3.8. Chemistry

3.8.1. General

Materials and reagents were purchased from Sigma-Aldrich and BLDpharm. For the synthesis and purification of the hit compounds, all the utilized solvents were analytically pure and dry. Thin-layer chromatography was performed using aluminum sheets coated with silica gel 60 F254 (Merck, Darmstadt, Germany). The compounds were purified using medium-pressure chromatography (MPLC) with columns containing silica gel Biotage® (Biotage, Uppsala, Sweden) SNAP ultra-HP-sphere 25 μm as stationary phase.

The purity of the virtual screening hits was assessed using high-pressure liquid chromatography (HPLC). The HPLC system consisted of two LC-10AD pumps and a SIL-HT autosampler from the manufacturer Shimadzu (Kyoto, Japan) and a SPD-M10A VP PDA detector. The UV absorbance of the sample was measured at 254 nm. Merck LiChrospher 100 RP18, 125 mm × 4 mm, 5 μm column was used as a stationary phase. The mobile phase for **hit-1** was composed of acetonitrile, H_2O, and 0.05 % trifluroacetic acid, while for **hit-2** the mobile phase was composed of methanol, H_2O, and 0.05 % trifluroacetic acid.

Varian NMR spectrometers 400/500 (Varian, Darmstadt, Deutschland) were used to measure ^{1}HNMR and ^{13}CNMR spectra using deuterated dimethyl sulfoxide (DMSO-d_6) as solvent. Chemical shifts

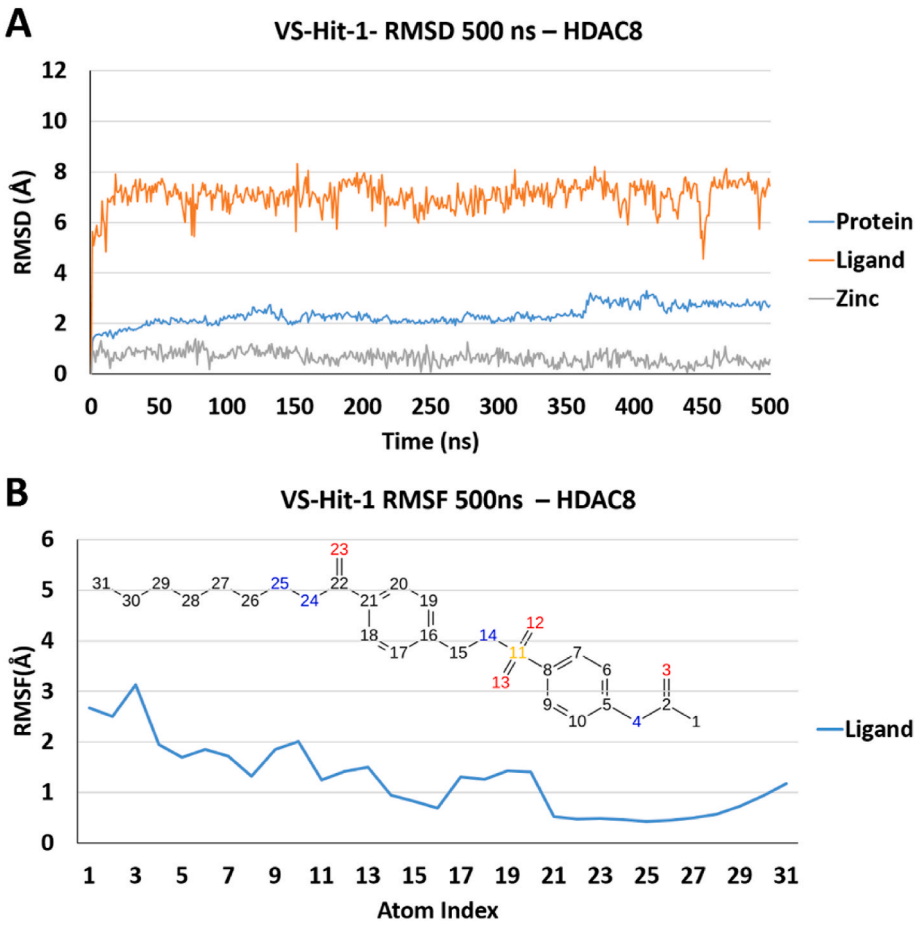

Fig. 14. (**A**). RMSD plots of the protein backbone, the ligand heavy atoms and the zinc ion of **hit-1** in HDAC8 from the long (500 ns) MD simulation. (**B**). RMSF plot of the ligand heavy atoms of **hit-1** in HDAC8 from the long (500 ns) MD simulation.

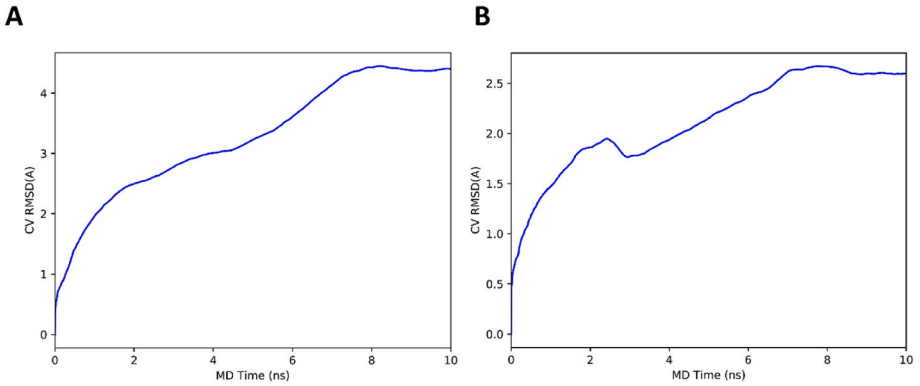

Fig. 15. Plots of the average collective variable (RMSD) over the BPMD simulation. (**A**) and (**B**). The starting docking pose and the shifted pose from last frame of the 500 ns MD simulation of **hit-1** in HDAC8, respectively.

were referenced to the residual solvent signals. High-resolution mass spectrometry (HRMS-ESI) analyses were performed with an LTQ (linear ion trap) Orbitrap XL hybrid mass spectrometer (Thermo Fisher Scientific).

3.8.2. *Synthesis procedures*

3.8.2.1. Methyl 4-[(4-acetamidobenzenesulfonamido)methyl]benzoate (3). A mixture of N-acetylsulfanilyl chloride **1** (2.34 g, 10 mmol), methyl 4-(aminomethyl)benzoate hydrochloride **2** (2.02 g, 10 mmol) and DIPEA (2.84 g, 22 mmol) in dichloromethane was stirred at room temperature for 1 h. 1 M HCl was then added to the mixture and the formed precipitate was filtered and dried. ^{1}H NMR (402 MHz, DMSO-d_6) δ 10.28 (s, 1H), 8.08 (t, J = 6.4 Hz, 1H), 7.85–7.81 (m, 2H), 7.72–7.65 (m, 4H), 7.35 (d, J = 8.4 Hz, 2H), 4.00 (d, J = 6.4 Hz, 2H), 3.80 (s, 3H), 2.05 (s, 3H). White solid, yield 74.5 %.

3.8.2.2. Methyl 4-[(2-methyl-1H-1,3-benzodiazol-1-yl)methyl]benzoate (8). A mixture of 2-methylbenzimidazol **6** (1.32 g, 10 mmol), methyl 4-(bromomethyl)benzoate **7** (2.29 g, 10 mmol) and DIPEA (1.29 g, 10 mmol) in dichloromethane was stirred at 50 °C overnight. The solvent was then evaporated. The remaining residue was dissolved in DMSO and

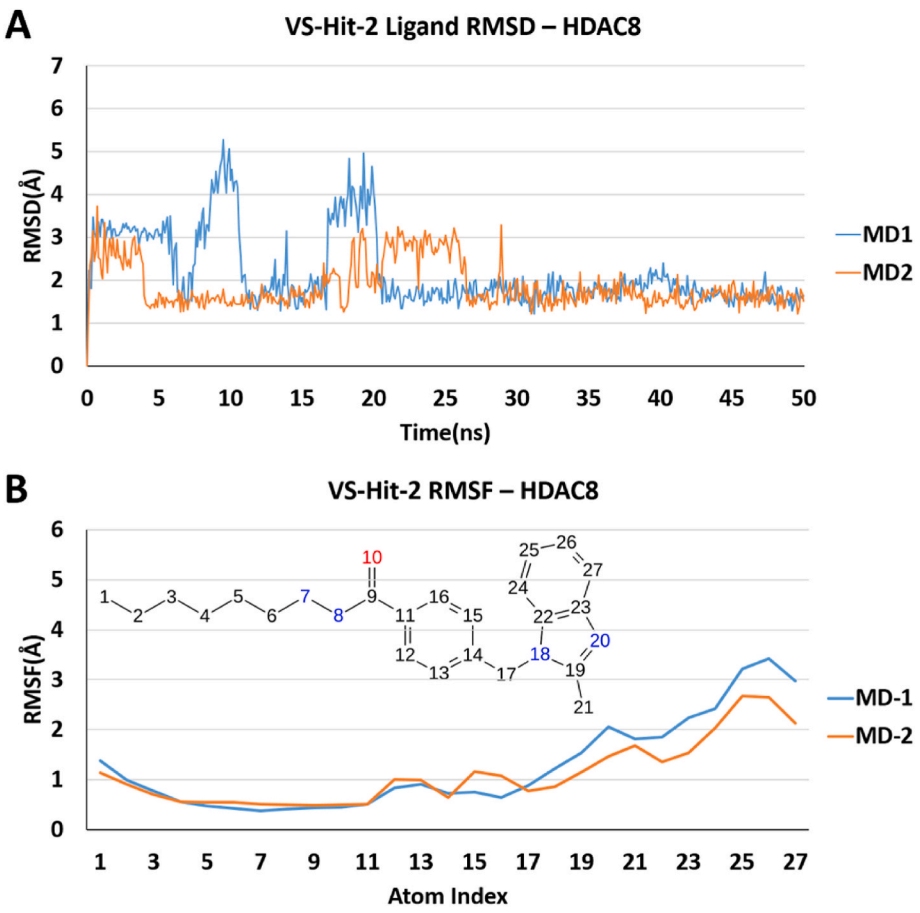

Fig. 16. (**A**) and (**B**). RMSD and RMSF plots, respectively, of ligand heavy atoms of **hit-2** in HDAC8 for two 50 ns independent MD simulations.

added dropwise to iced water. The formed precipitate was then filtered and dried. ^{1}H NMR (402 MHz, DMSO-d_6) δ 8.00–7.79 (m, 2H), 7.55–7.50 (m, 1H), 7.41–7.37 (m, 1H), 7.19 (d, J = 8.3 Hz, 2H), 7.13–7.09 (m, 2H), 5.53 (s, 2H), 3.78 (s, 3H), 2.46 (s, 3H). White solid, yield 62.43 %.

3.8.2.3. General procedure for synthesis of acid hydrazides (4 and 9). The respective ester derivative **3** or **8** (1 eq.) was dissolved in a mixture of hydrazine monohydrate (30 eq.) and ethanol (3 mL). The mixture was heated under reflux for 2 h, after which it was left to cool. The formed precipitate was then filtered and dried.

3.8.2.3.1. N-[4-({[4-(Hydrazinecarbonyl)phenyl]methyl}sulfamoyl) phenyl]acetamide (4). ^{1}H NMR (402 MHz, DMSO-d_6) δ 10.26 (s, 1H), 9.67 (s, 1H), 8.02 (t, J = 6.3 Hz, 1H), 7.76–7.65 (m, 6H), 7.27 (d, J = 8.2 Hz, 2H), 4.43 (s, 2H), 3.95 (d, J = 6.1 Hz, 2H), 2.05 (s, 3H). White solid, yield 82.78 %.

3.8.2.3.2. 4-[(2-Methyl-1H-1,3-benzodiazol-1-yl)methyl]benzohydrazide (9). ^{1}H NMR (402 MHz, DMSO-d_6) δ 9.67 (s, 1H), 7.72 (d, J = 8.3 Hz, 2H), 7.54–7.49 (m, 1H), 7.43–7.37 (m, 1H), 7.15–7.08 (m, 4H), 5.48 (s, 2H), 4.42 (s, 2H), 2.47 (s, 3H). White solid, yield 88.56 %.

3.8.2.4. General procedure for synthesis of alkyl hydrazides (5 and 10). A mixture of the respective acid hydrazide **4** or **9** (1 eq.), hexanal (1 eq.) and *p*-toluene sulfonic acid (pTSA) (catalytic amount) was stirred in methanol (10 mL) at room temperature for 1 h. Sodium borohydride (4 eq.) was then added portion wise over 4 h. The reaction mixture was then diluted with water and extracted with ethyl acetate. The organic layer was dried on anhydrous sodium sulphate and evaporated under vacuum. The product was purified by medium pressure liquid chromatography (MPLC) using a gradient of dichloromethane and methanol.

3.8.2.4.1. N-[4-({[4-(N′-Hexylhydrazinecarbonyl)phenyl]methyl}sulfamoyl)phenyl]acetamide (5, hit-1). ^{1}H NMR (402 MHz, DMSO-d_6) δ 10.26 (s, 1H), 9.91 (s, 1H), 8.02 (t, J = 6.2 Hz, 1H), 7.75–7.65 (m, 6H), 7.27 (d, J = 8.2 Hz, 2H), 5.02 (s, 1H), 3.96 (d, J = 6.2 Hz, 2H), 2.72 (t, J = 7.0 Hz, 2H), 2.05 (s, 3H), 1.44–1.35 (m, 2H), 1.32–1.17 (m, 6H), 0.82 (t, J = 6.7 Hz, 3H). ^{13}C NMR (101 MHz, DMSO-d_6) δ 169.37, 165.36, 143.19, 141.56, 134.61, 132.43, 128.08, 127.72, 127.39, 119.04, 51.64, 46.13, 31.63, 28.01, 26.76, 24.55, 22.50, 14.35. HRMS *m/z*: $[M + H]^+$ found: 447.2057; calculated $C_{22}H_{31}N_4O_4S$: 447.2066. White solid, yield 17 %

3.8.2.4.2. N′-Hexyl-4-[(2-methyl-1H-1,3-benzodiazol-1-yl)methyl] benzohydrazide (10, hit-2). ^{1}H NMR (402 MHz, DMSO-d_6) δ 9.91 (s, 1H), 7.72 (d, J = 8.3 Hz, 2H), 7.56–7.48 (m, 1H), 7.42–7.36 (m, 1H), 7.19–7.07 (m, 4H), 5.48 (s, 2H), 5.00 (s, 1H), 2.70 (t, J = 7.0 Hz, 2H), 2.47 (s, 3H), 1.43–1.33 (m, 2H), 1.31–1.16 (m, 6H), 0.81 (t, J = 6.8 Hz, 3H). ^{13}C NMR (126 MHz, DMSO-d_6) δ 165.30, 152.31, 142.84, 140.59, 135.74, 132.96, 127.95, 126.95, 122.11, 121.82, 118.78, 110.41, 51.62, 46.42, 31.64, 28.02, 26.76, 22.51, 14.36, 14.05. HRMS *m/z*: $[M + H]^+$ found: 365.2334; calculated $C_{22}H_{29}N_4O$: 365.2341.White solid, yield 42.5 %

3.9. HDAC in vitro evaluation

As previously reported, human HDAC11 full-length protein was expressed and purified and used for the current study [18]. To measure HDAC11 inhibition in vitro a fluorescence based enzymatic assay was applied [17]. For this a PerkinElmer Envision 2104 multilabel plate reader (Waltham, MA, USA) was used at λex = 320 nm and λem = 430 nm. The reaction mixture consisted of HDAC11, and the acylated peptide substrate derived from TNFα in a reaction buffer comprising 20 mM

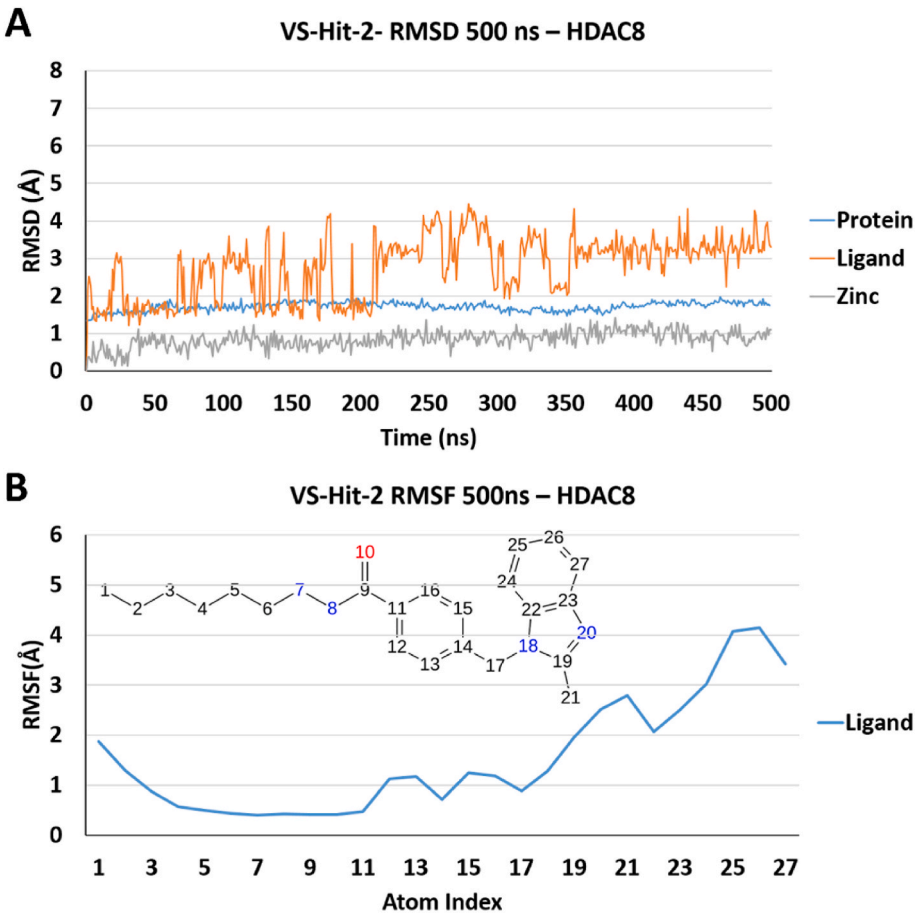

Fig. 17. (**A**). RMSD plots of the protein backbone, the ligand heavy atoms and the zinc ion of **hit-2** in HDAC8 from the long (500 ns) MD simulation. (**B**). RMSF plot of the ligand heavy atoms of **hit-2** in HDAC8 from the long (500 ns) MD simulation.

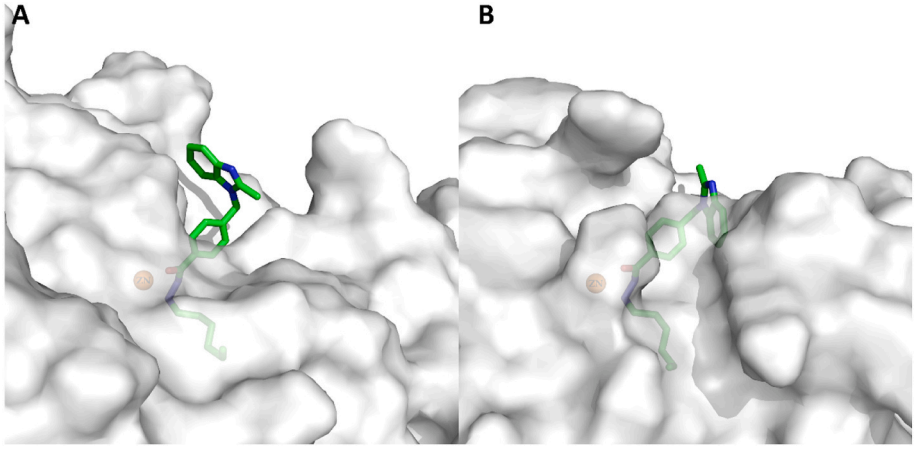

Fig. 18. Highlight of the effect of longer loop-1 in HDAC11 on the binding site shape and ligand exposure to solvent. (**A**) and (**B**). The docking poses of the **hit-2** in HDAC8 and HDAC11, respectively. The protein appears as white surface and the ligand as green sticks. (For interpretation of the references to colour in this figure legend, the reader is referred to the Web version of this article.)

HEPES, 2 mg/mL BSA, and 70 μMTCEP, and at pH 7.4 which was adjusted with NaOH (total volume 40 μL) [17]. All reactions were incubated in 384-well plates for 30 min at room temperature, and the increase of relative fluorescence reflecting the product formation was monitored. The fluorescence increase was followed for 1 h with two reads per min. As reference we used the reported compound SIS17 (purchased from MedChemExpress LLC, 1 Deer Park Dr, Suite Q, Monmouth Junction, NJ 08852, USA).

For HDAC1, 2, 3 and HDAC6 recombinant proteins were purchased from ENZO Life Sciences AG (Lausen, CH) whereas HDAC4, 5, 7, 8, 9 and 10 were produced as reported before [107,108]. All inhibitors were tested using 384-well plates (GreinerONe, catalogue no. 784900) [17, 108]. After 5 min of incubation of the inhibitors with the respective enzymes (HDAC1 = 10 nM, HDAC2 and HDAC3 = 3 nM, HDAC4 = 5 nM, HDAC5 = 10 nM, HDAC6 = 1 nM, HDAC7 = 5 nM, HDAC8 = 2 nM, HDAC9 = 20 nM, HDAC10 = 5 nM), the reactions were started by the

addition of the substrates described below.

For HDAC1, 2, 3 and 6, an acetylated peptide substrate derived from p53 (Ac-RHKK(Acetyl)-AMC) was used in a discontinuous fluorescence assay [107]. The reactions were performed in assay buffer (20 mM HEPES, 140 mM NaCl, 10 mM $MgCl_2$, 1 mM TCEP and 0.2 mg/mL BSA, pH 7.4 adjusted with NaOH). HDAC1 was incubated at 37 °C for 90 min. HDAC2 and HDAC3 were incubated for 1h at RT and HDAC6 for 30 min at RT. The reaction was quenched after 1 h by adding trypsin and SAHA. The fluorescence intensity was measured after 1 h of incubation using an Envision 2104 Multilabel Plate Reader (PerkinElmer, Waltham, MA), with an excitation wavelength of 380 ± 8 nm and an emission wavelength of 430 ± 8 nm. HDAC4, 5, 7, 8 and 9 were measured in a continuous manner using the thio-acetylated peptide substrate (Abz-SRGGK(thio-TFA)FFRR-NH_2) [107]. For HDAC10, an internal quenched spermidine-like substrate was utilized. The fluorescence increase was followed for 1 h with two reads per min with an excitation wavelength of 320 ± 8 nm and an emission wavelength of 430 ± 8 nm. All tests were done in three replicates.

4. Conclusion

In the present study, a categorical classification model was developed and successfully integrated into a ligand-based virtual screening workflow to identify new potent HDAC11 inhibitors. For the virtual screening, a focused library of alkyl hydrazide compounds from the ZINC20 library was tailored to meet the optimal structural requirements for HDAC11 inhibition by replacing the N′-alkyl substituents with an N′-hexyl group. The two best hits were synthesized and evaluated through in vitro enzymatic assays. Both compounds exhibited strong inhibition of HDAC11, with IC_{50} values of 172.19 nM for **hit-1** and 21.98 nM for **hit-2**. Additionally, the compounds selectively inhibited HDAC11 at a concentration of 1 μM over other HDAC subtypes, except for HDAC8, for which strong inhibition was also observed.

The binding mode of the identified hits in HDAC11 was predicted through docking and further investigated using short and long MD simulations. The MD simulation results demonstrated a stabilized pose of **hit-1**, in which the sulfonamide linker shifts its position in the opposite direction of the HDAC11 pocket opening to form additional hydrogen bonds with His35, Glu94, and Tyr304. For **hit-2**, a very high stability of the ligand during the simulation was confirmed, as evidenced by the RMSD and RMSF plots of the ligand heavy atoms and the persistence of interactions. Furthermore, binding pose metadynamics verified the results from the MD simulations of **hit-1** by confirming the greater stability of the equilibrated ligand pose compared to the initial docking pose in terms of PoseScore, PersScore, and CompScore. Additionally, the binding mode of the identified hits in HDAC8 was investigated by molecular docking followed by further verification through short and long classical MD simulations, as well as metadynamics. The results demonstrated different binding modes and behavior of the ligands in HDAC8 compared to those observed in HDAC11, therefore highlighting the effect of the structural differences between the two isoforms on ligand binding and dynamics.

While the strategy employed in this study successfully led to the identification of new potent HDAC11 inhibitors, the compounds did not exhibit absolute selectivity for HDAC11, as strong inhibition of HDAC8 was also observed. Therefore, as a future perspective, optimization of the identified compounds will be pursued to further enhance their selectivity for HDAC11.

CRediT authorship contribution statement

Fady Baselious: Writing – original draft, Visualization, Software, Methodology, Investigation, Formal analysis. **Sebastian Hilscher:** Software, Methodology, Investigation. **Lukas Handke:** Investigation, Formal analysis. **Cyril Barinka:** Methodology, Investigation. **Mike Schutkowski:** Writing – review & editing, Supervision. **Wolfgang Sippl:** Writing – review & editing, Supervision, Resources, Data curation, Conceptualization.

Ethics in publishing statement

This research presents an accurate account of the work performed, all data presented are accurate and methodologies detailed enough to permit others to replicate the work.

This manuscript represents entirely original works and or if work and/or words of others have been used, that this has been appropriately cited or quoted and permission has been obtained where necessary.

This material has not been published in whole or in part elsewhere.

The manuscript is not currently being considered for publication in another journal.

That generative AI and AI-assisted technologies have not been utilized in the writing process or if used, disclosed in the manuscript the use of AI and AI-assisted technologies and a statement will appear in the published work.

That generative AI and AI-assisted technologies have not been used to create or alter images unless specifically used as part of the research design where such use must be described in a reproducible manner in the methods section.

All authors have been personally and actively involved in substantive work leading to the manuscript and will hold themselves jointly and individually responsible for its content.

Funding

This work was in part supported by the CAS (RVO: 86652036) and the Grant Agency of the Czech Republic (24-12155S) (C.B.).

Declaration of competing interest

The authors declare that they have no known competing financial interests or personal relationships that could have appeared to influence the work reported in this paper.

Acknowledgement

This work was funded by the Deutsche Forschungsgemeinschaft (DFG) project numbers 469954457 and 503267011 (to W.S).

Appendix A. Supplementary data

Supplementary data to this article can be found online at https://doi.org/10.1016/j.compbiomed.2025.110695.

References

[1] P.M. Lombardi, K.E. Cole, D.P. Dowling, D.W. Christianson, Structure, mechanism, and inhibition of histone deacetylases and related metalloenzymes, Curr. Opin. Struct. Biol. 21 (6) (2011) 735–743, https://doi.org/10.1016/j.sbi.2011.08.004.

[2] G. Milazzo, D. Mercatelli, G. Di Muzio, L. Triboli, P. De Rosa, G. Perini, F. M. Giorgi, Histone deacetylases (HDACs): Evolution, specificity, role in transcriptional complexes, and pharmacological actionability, Genes 11 (5) (2020), https://doi.org/10.3390/genes11050556.

[3] L. Gao, M.A. Cueto, F. Asselbergs, P. Atadja, Cloning and functional characterization of HDAC11, a novel member of the human histone deacetylase family, J. Biol. Chem. 277 (28) (2002) 25748–25755, https://doi.org/10.1074/jbc.M111871200.

[4] Y. Núñez-Álvarez, M. Suelves, HDAC11: a multifaceted histone deacetylase with proficient fatty deacylase activity and its roles in physiological processes, FEBS J. 289 (10) (2022) 2771–2792, https://doi.org/10.1111/febs.15895.

[5] J. Cao, L. Sun, P. Aramsangtienchai, N.A. Spiegelman, X. Zhang, W. Huang, E. Seto, H. Lin, HDAC11 regulates type I interferon signaling through defatty-acylation of SHMT2, Proc. Natl. Acad. Sci. 116 (12) (2019) 5487–5492, https://doi.org/10.1073/pnas.1815365116.

[6] A. Villagra, F. Cheng, H.W. Wang, I. Suarez, M. Glozak, M. Maurin, D. Nguyen, K. L. Wright, P.W. Atadja, K. Bhalla, J. Pinilla-Ibarz, E. Seto, E.M. Sotomayor, The histone deacetylase HDAC11 regulates the expression of interleukin 10 and

immune tolerance, Nat. Immunol. 10 (1) (2009) 92–100, https://doi.org/10.1038/ni.1673.
[7] D. Gong, Z. Zeng, F. Yi, J. Wu, Inhibition of histone deacetylase 11 promotes human liver cancer cell apoptosis, Am J Transl Res 11 (2) (2019) 983–990.
[8] W. Wang, L. Fu, S. Li, Z. Xu, X. Li, Histone deacetylase 11 suppresses p53 expression in pituitary tumor cells, Cell Biol. Int. 41 (12) (2017) 1290–1295, https://doi.org/10.1002/cbin.10834.
[9] Y.L. Wu, Z.J. Lin, C.C. Li, X. Lin, S.K. Shan, B. Guo, M.H. Zheng, F. Li, L.Q. Yuan, Z.H. Li, Epigenetic regulation in metabolic diseases: mechanisms and advances in clinical study, Signal Transduct. Targeted Ther. 8 (1) (2023) 98, https://doi.org/10.1038/s41392-023-01333-7.
[10] H. Yang, L. Chen, Q. Sun, F. Yao, S. Muhammad, C. Sun, The role of HDAC11 in obesity-related metabolic disorders: a critical review, J. Cell. Physiol. 236 (8) (2021) 5582–5591, https://doi.org/10.1002/jcp.30286.
[11] H. Chen, C. Xie, Q. Chen, S. Zhuang, HDAC11, an emerging therapeutic target for metabolic disorders, Front. Endocrinol. 13 (2022) 989305, https://doi.org/10.3389/fendo.2022.989305.
[12] H. Yang, C. Li, M. Che, J. Liang, X. Tian, G. Yang, C. Sun, HDAC11 deficiency resists obesity by converting adipose-derived stem cells into brown adipocyte-like cells, Int. J. Biol. Macromol. 258 (Pt 1) (2024) 128852, https://doi.org/10.1016/j.ijbiomac.2023.128852.
[13] M.W. Martin, J.Y. Lee, D.R. Lancia Jr., P.Y. Ng, B. Han, J.R. Thomason, M. S. Lynes, C.G. Marshall, C. Conti, A. Collis, M.A. Morales, K. Doshi, A. Rudnitskaya, L. Yao, X. Zheng, Discovery of novel N-hydroxy-2-arylisoindoline-4-carboxamides as potent and selective inhibitors of HDAC11, Bioorg. Med. Chem. Lett. 28 (12) (2018) 2143–2147, https://doi.org/10.1016/j.bmcl.2018.05.021.
[14] N. Bora-Singhal, D. Mohankumar, B. Saha, C.M. Colin, J.Y. Lee, M.W. Martin, X. Zheng, D. Coppola, S. Chellappan, Novel HDAC11 inhibitors suppress lung adenocarcinoma stem cell self-renewal and overcome drug resistance by suppressing Sox 2, Sci. Rep. 10 (1) (2020) 4722, https://doi.org/10.1038/s41598-020-61295-6.
[15] P. Bai, Y. Liu, L. Yang, W. Ding, P. Mondal, N. Sang, G. Liu, X. Lu, T.T. Ho, Y. Zhou, R. Wu, V.C. Birar, M.Q. Wilks, R.E. Tanzi, H. Lin, C. Zhang, W. Li, S. Shen, C. Wang, Development and pharmacochemical characterization discover a novel brain-permeable HDAC11-Selective inhibitor with therapeutic potential by regulating neuroinflammation in mice, J. Med. Chem. 66 (23) (2023) 16075–16090, https://doi.org/10.1021/acs.jmedchem.3c01491.
[16] F. Baselious, S. Hilscher, S. Hagemann, S. Tripathee, D. Robaa, C. Barinka, S. Hüttelmaier, M. Schutkowski, W. Sippl, Utilization of an optimized AlphaFold protein model for structure-based design of a selective HDAC11 inhibitor with anti-neuroblastoma activity, Arch Pharm (Weinheim) 357 (10) (2024) e2400486, https://doi.org/10.1002/ardp.202400486.
[17] F. Baselious, S. Hilscher, D. Robaa, C. Barinka, M. Schutkowski, W. Sippl, Comparative structure-based virtual screening utilizing optimized AlphaFold model identifies selective HDAC11 inhibitor, Int. J. Mol. Sci. 25 (2024).
[18] Z. Kutil, Z. Novakova, M. Meleshin, J. Mikesova, M. Schutkowski, C. Barinka, Histone deacetylase 11 is a fatty-acid deacylase, ACS Chem. Biol. 13 (3) (2018) 685–693, https://doi.org/10.1021/acschembio.7b00942.
[19] C. Moreno-Yruela, I. Galleano, A.S. Madsen, C.A. Olsen, Histone deacetylase 11 is an ε-N-Myristoyllysine hydrolase, Cell Chem. Biol. 25 (7) (2018) 849–856.e848, https://doi.org/10.1016/j.chembiol.2018.04.007.
[20] Z. Kutil, J. Mikešová, M. Zessin, M. Meleshin, Z. Nováková, G. Alquicer, A. Kozikowski, W. Sippl, C. Bařinka, M. Schutkowski, Continuous activity assay for HDAC11 enabling reevaluation of HDAC inhibitors, ACS Omega 4 (22) (2019) 19895–19904, https://doi.org/10.1021/acsomega.9b02808.
[21] S.I. Son, J. Cao, C.L. Zhu, S.P. Miller, H. Lin, Activity-guided design of HDAC11-Specific inhibitors, ACS Chem. Biol. 14 (7) (2019) 1393–1397, https://doi.org/10.1021/acschembio.9b00292.
[22] T.T. Ho, C. Peng, E. Seto, H. Lin, Trapoxin A analogue as a selective nanomolar inhibitor of HDAC11, ACS Chem. Biol. 18 (4) (2023) 803–809, https://doi.org/10.1021/acschembio.2c00840.
[23] R. De Vreese, M. D'Hooghe, Synthesis and applications of benzohydroxamic acid-based histone deacetylase inhibitors, Eur. J. Med. Chem. 135 (2017) 174–195, https://doi.org/10.1016/j.ejmech.2017.04.013.
[24] L. Zhang, J. Zhang, Q. Jiang, L. Zhang, W. Song, Zinc binding groups for histone deacetylase inhibitors, J. Enzym. Inhib. Med. Chem. 33 (1) (2018) 714–721, https://doi.org/10.1080/14756366.2017.1417274.
[25] Y. Sun, Y. Sun, S. Yue, Y. Wang, F. Lu, Histone deacetylase inhibitors in cancer therapy, Curr. Top. Med. Chem. 18 (28) (2018) 2420–2428, https://doi.org/10.2174/1568026619666181210152115.
[26] B.S. Mann, J.R. Johnson, M.H. Cohen, R. Justice, R. Pazdur, FDA approval summary: vorinostat for treatment of advanced primary cutaneous T-cell lymphoma, Oncologist 12 (10) (2007) 1247–1252, https://doi.org/10.1634/theoncologist.12-10-1247.
[27] H.Z. Lee, V.E. Kwitkowski, P.L. Del Valle, M.S. Ricci, H. Saber, B.A. Habtemariam, J. Bullock, E. Bloomquist, Y. Li Shen, X.H. Chen, J. Brown, N. Mehrotra, S. Dorff, R. Charlab, R.C. Kane, E. Kaminskas, R. Justice, A.T. Farrell, R. Pazdur, FDA approval: Belinostat for the treatment of patients with relapsed or refractory peripheral T-cell lymphoma, Clin. Cancer Res. 21 (12) (2015) 2666–2670, https://doi.org/10.1158/1078-0432.Ccr-14-3119.
[28] J.P. Laubach, P. Moreau, J.F. San-Miguel, P.G. Richardson, Panobinostat for the treatment of multiple myeloma, Clin. Cancer Res. 21 (21) (2015) 4767–4773, https://doi.org/10.1158/1078-0432.Ccr-15-0530.
[29] H. Wang, N. Yu, D. Chen, K.C. Lee, P.L. Lye, J.W. Chang, W. Deng, M.C. Ng, T. Lu, M.L. Khoo, A. Poulsen, K. Sangthongpitag, X. Wu, C. Hu, K.C. Goh, X. Wang, L. Fang, K.L. Goh, H.H. Khng, S.K. Goh, P. Yeo, X. Liu, Z. Bonday, J.M. Wood, B. W. Dymock, E. Kantharaj, E.T. Sun, Discovery of (2E)-3-{2-butyl-1-[2-(diethylamino)ethyl]-1H-benzimidazol-5-yl}-N-hydroxyacrylamide (SB939), an orally active histone deacetylase inhibitor with a superior preclinical profile, J. Med. Chem. 54 (13) (2011) 4694–4720, https://doi.org/10.1021/jm2003552.
[30] X. Cai, H.X. Zhai, J. Wang, J. Forrester, H. Qu, L. Yin, C.J. Lai, R. Bao, C. Qian, Discovery of 7-(4-(3-ethynylphenylamino)-7-methoxyquinazolin-6-yloxy)-N-hydroxyheptanamide (CUDc-101) as a potent multi-acting HDAC, EGFR, and HER2 inhibitor for the treatment of cancer, J. Med. Chem. 53 (5) (2010) 2000–2009, https://doi.org/10.1021/jm901453q.
[31] G.J. Ossenkoppele, B. Lowenberg, P. Zachee, N. Vey, D. Breems, A.A. Van de Loosdrecht, A.H. Davidson, G. Wells, L. Needham, L. Bawden, M. Toal, L. Hooftman, P.M. Debnam, A phase I first-in-human study with tefinostat - a monocyte/macrophage targeted histone deacetylase inhibitor - in patients with advanced haematological malignancies, Br. J. Haematol. 162 (2) (2013) 191–201, https://doi.org/10.1111/bjh.12359.
[32] P. Huang, I. Almeciga-Pinto, M. Jarpe, J.H. van Duzer, R. Mazitschek, M. Yang, S. S. Jones, S.N. Quayle, Selective HDAC inhibition by ACY-241 enhances the activity of paclitaxel in solid tumor models, Oncotarget 8 (2) (2017) 2694–2707, https://doi.org/10.18632/oncotarget.13738.
[33] I. Becher, T. Werner, C. Doce, E.A. Zaal, I. Tögel, C.A. Khan, A. Rueger, M. Muelbaier, E. Salzer, C.R. Berkers, P.F. Fitzpatrick, M. Bantscheff, M. M. Savitski, Thermal profiling reveals phenylalanine hydroxylase as an off-target of panobinostat, Nat. Chem. Biol. 12 (11) (2016) 908–910, https://doi.org/10.1038/nchembio.2185.
[34] S. Lechner, M.I.P. Malgapo, C. Grätz, R.R. Steimbach, A. Baron, P. Rüther, S. Nadal, C. Stumpf, C. Loos, X. Ku, P. Prokofeva, L. Lautenbacher, T. Heimburg, V. Würf, C. Meng, M. Wilhelm, W. Sippl, K. Kleigrewe, J.K. Pauling, K. Kramer, A. K. Miller, M.W. Pfaffl, M.E. Linder, B. Kuster, G. Médard, Target deconvolution of HDAC pharmacopoeia reveals MBLAC2 as common off-target, Nat. Chem. Biol. 18 (8) (2022) 812–820, https://doi.org/10.1038/s41589-022-01015-5.
[35] A. Baumann, N. Papenkordt, D. Robaa, P.D. Szigetvari, A. Vogelmann, F. Bracher, W. Sippl, M. Jung, J. Haavik, Aromatic amino acid hydroxylases as off-targets of histone deacetylase inhibitors, ACS Chem. Neurosci. 15 (22) (2024) 4143–4155, https://doi.org/10.1021/acschemneuro.4c00346.
[36] S. Shen, A.P. Kozikowski, Why hydroxamates may not be the best histone deacetylase inhibitors—what some may have forgotten or would rather forget? ChemMedChem 11 (1) (2016) 15–21, https://doi.org/10.1002/cmdc.201500486.
[37] G.F. Smith, Designing drugs to avoid toxicity, in: G. Lawton, D.R. Witty (Eds.), Progress in Medicinal Chemistry, vol. 50, Elsevier, 2011, pp. 1–47.
[38] L.Z. Wang, J. Ramírez, W. Yeo, M.Y. Chan, W.L. Thuya, J.Y. Lau, S.C. Wan, A. L. Wong, Y.K. Zee, R. Lim, S.C. Lee, P.C. Ho, H.S. Lee, A. Chan, S. Ansher, M. J. Ratain, B.C. Goh, Glucuronidation by UGT1A1 is the dominant pathway of the metabolic disposition of belinostat in liver cancer patients, PLoS One 8 (1) (2013) e54522, https://doi.org/10.1371/journal.pone.0054522.
[39] S.P. Kang, J. Ramirez, L. House, W. Zhang, S. Mirkov, W. Liu, E. Haverfield, M. J. Ratain, A pharmacogenetic study of vorinostat glucuronidation, Pharmacogenet. Genom. 20 (10) (2010) 638–641, https://doi.org/10.1097/FPC.0b013e32833e1b37.
[40] R.M. Balliet, G. Chen, C.J. Gallagher, R.W. Dellinger, D. Sun, P. Lazarus, Characterization of UGTs active against SAHA and association between SAHA glucuronidation activity phenotype with UGT genotype, Cancer Res. 69 (7) (2009) 2981–2989, https://doi.org/10.1158/0008-5472.CAN-08-4143.
[41] H.S. Ibrahim, M. Abdelsalam, Y. Zeyn, M. Zessin, A.M. Mustafa, M.A. Fischer, P. Zeyen, P. Sun, E.F. Bülbül, A. Vecchio, F. Erdmann, M. Schmidt, D. Robaa, C. Barinka, C. Romier, M. Schutkowski, O.H. Krämer, W. Synthesis Sippl, Molecular docking and biological characterization of pyrazine linked 2-Amino-benzamides as new class I selective histone deacetylase (HDAC) inhibitors with anti-leukemic activity, Int. J. Mol. Sci. 23 (1) (2021) 369, https://doi.org/10.3390/ijms23010369.
[42] P. Sun, J. Wang, K.S. Khan, W. Yang, B.W.-L. Ng, N. Ilment, M. Zessin, E.F. Bülbül, D. Robaa, F. Erdmann, M. Schmidt, C. Romier, M. Schutkowski, A.S.-L. Cheng, W. Sippl, Development of alkylated hydrazides as highly potent and selective class I histone deacetylase inhibitors with T cell modulatory properties, J. Med. Chem. 65 (24) (2022) 16313–16337, https://doi.org/10.1021/acs.jmedchem.2c01132.
[43] F. Berluti, F. Baselious, S. Hagemann, S. Hilscher, M. Schmidt, S. Hüttelmaier, M. Schutkowski, W. Sippl, H.S. Ibrahim, Development of new pyrazoles as class I HDAC inhibitors: synthesis, molecular modeling, and biological characterization in leukemia cells, Arch. Pharmazie 357 (11) (2024) e2400437, https://doi.org/10.1002/ardp.202400437.
[44] S. Li, Z. Hu, W. Pan, H. Wu, W. Peng, Y. Wu, F. Jiang, X. Peng, Discovery of highly potent and orally bioavailable histone deacetylase 3 inhibitors as immunomodulators and enhancers of DNA-damage response in cancer therapy, J. Med. Chem. 68 (3) (2025) 3212–3237, https://doi.org/10.1021/acs.jmedchem.4c02445.
[45] D. Stopper, L. Biermann, P.R. Watson, J. Li, B. König, M.N. Gaynes, L. Pessanha de Carvalho, J. Klose, M. Hanl, A. Hamacher, L. Schäker-Hübner, D. Ramsbeck, J. Held, D.W. Christianson, M.U. Kassack, F.K. Hansen, Exploring alternative zinc-binding groups in histone deacetylase (HDAC) inhibitors uncovers DS-103 as a potent Ethylhydrazide-Based HDAC inhibitor with chemosensitizing properties, J. Med. Chem. (2025), https://doi.org/10.1021/acs.jmedchem.4c02373.
[46] W.P. Walters, M.T. Stahl, M.A. Murcko, Virtual Screening—an overview, Drug Discov. Today 3 (4) (1998) 160–178, https://doi.org/10.1016/S1359-6446(97)01163-X.

[47] A. Lavecchia, C. Di Giovanni, Virtual screening strategies in drug discovery: a critical review, Curr. Med. Chem. 20 (23) (2013) 2839–2860, https://doi.org/10.2174/09298673113209990001.

[48] A.V. Sadybekov, V. Katritch, Computational approaches streamlining drug discovery, Nature 616 (7958) (2023) 673–685, https://doi.org/10.1038/s41586-023-05905-z.

[49] J.J. Irwin, K.G. Tang, J. Young, C. Dandarchuluun, B.R. Wong, M. Khurelbaatar, Y.S. Moroz, J. Mayfield, R.A. Sayle, ZINC20—A free ultralarge-scale chemical database for ligand discovery, J. Chem. Inf. Model. 60 (12) (2020) 6065–6073, https://doi.org/10.1021/acs.jcim.0c00675.

[50] S. Kralj, M. Jukič, U. Bren, Molecular filters in medicinal chemistry, Encyclopedia 3 (2) (2023) 501–511, https://doi.org/10.3390/encyclopedia3020035.

[51] C.A. Lipinski, Drug-like properties and the causes of poor solubility and poor permeability, J. Pharmacol. Toxicol. Methods 44 (1) (2000) 235–249, https://doi.org/10.1016/s1056-8719(00)00107-6.

[52] W.P. Walters, M.A. Murcko, Prediction of 'drug-likeness', Adv. Drug Deliv. Rev. 54 (3) (2002) 255–271, https://doi.org/10.1016/s0169-409x(02)00003-0.

[53] W.P. Walters, M. Namchuk, Designing screens: how to make your hits a hit, Nat. Rev. Drug Discov. 2 (4) (2003) 259–266, https://doi.org/10.1038/nrd1063.

[54] C.A. Lipinski, F. Lombardo, B.W. Dominy, P.J. Feeney, Experimental and computational approaches to estimate solubility and permeability in drug discovery and development settings, Adv. Drug Deliv. Rev. 46 (1–3) (2001) 3–26, https://doi.org/10.1016/s0169-409x(00)00129-0.

[55] S. Kumari, S. Chakraborty, M. Ahmad, V. Kumar, P.B. Tailor, B.K. Biswal, Identification of probable inhibitors for the DNA polymerase of the monkeypox virus through the virtual screening approach, Int. J. Biol. Macromol. 229 (2023) 515–528, https://doi.org/10.1016/j.ijbiomac.2022.12.252.

[56] A. Bender, Bayesian methods in virtual screening and chemical biology, in: J. Bajorath (Ed.), Chemoinformatics and Computational Chemical Biology, Humana Press, 2011, pp. 175–196.

[57] A. Lavecchia, Machine-learning approaches in drug discovery: methods and applications, Drug Discov. Today 20 (3) (2015) 318–331, https://doi.org/10.1016/j.drudis.2014.10.012.

[58] T.A. Oliveira, M.P. Silva, E.H. Maia, A.M. Silva, A.G. Taranto, Virtual screening algorithms in drug discovery: a review focused on machine and deep learning methods, Drugs Drug Candidates 2 (2023) 311–334.

[59] P. Watson, Naïve bayes classification using 2D pharmacophore feature triplet vectors, J. Chem. Inf. Model. 48 (1) (2008) 166–178, https://doi.org/10.1021/ci7003253.

[60] N.M. O'Boyle, R.A. Sayle, Comparing structural fingerprints using a literature-based similarity benchmark, J. Cheminf. 8 (1) (2016) 36, https://doi.org/10.1186/s13321-016-0148-0.

[61] M. Sastry, J.F. Lowrie, S.L. Dixon, W. Sherman, Large-scale systematic analysis of 2D fingerprint methods and parameters to improve virtual screening enrichments, J. Chem. Inf. Model. 50 (5) (2010) 771–784, https://doi.org/10.1021/ci100062n.

[62] D. Rogers, R.D. Brown, M. Hahn, Using extended-connectivity fingerprints with Laplacian-modified Bayesian analysis in high-throughput screening follow-up, J. Biomol. Screen 10 (7) (2005) 682–686, https://doi.org/10.1177/1087057105281365.

[63] D. Rogers, M. Hahn, Extended-connectivity fingerprints, J. Chem. Inf. Model. 50 (5) (2010) 742–754, https://doi.org/10.1021/ci100050t.

[64] P. De, S. Kar, P. Ambure, K. Roy, Prediction reliability of QSAR models: an overview of various validation tools, Arch. Toxicol. 96 (5) (2022) 1279–1295, https://doi.org/10.1007/s00204-022-03252-y.

[65] J. Devillers, Methods for building QSARs, in: B. Reisfeld, A.N. Mayeno (Eds.), Computational Toxicology: Volume II, Humana Press, 2013, pp. 3–27.

[66] A. Golbraikh, A. Tropsha, QSAR/QSPR revisited, in: T. Engel, J. Gasteiger (Eds.), Chemoinformatics: Basic Concepts and Methods, Wiley-VCH, 2018, pp. 465–495.

[67] L. Zhang, H. Zhu, T.I. Oprea, A. Golbraikh, A. Tropsha, QSAR modeling of the blood-brain barrier permeability for diverse organic compounds, Pharm. Res. 25 (8) (2008) 1902–1914, https://doi.org/10.1007/s11095-008-9609-0.

[68] W. Sippl, D. Robaa, QSAR/QSPR, in: T. Engel, J. Gasteiger (Eds.), Applied Chemoinformatics: Achievements and Future Opportunities, Wiley-VCH, 2018, pp. 9–52.

[69] K. Toutah, N. Nawar, S. Timonen, H. Sorger, Y.S. Raouf, S. Bukhari, J. von Jan, A. Ianevski, J.M. Gawel, O.O. Olaoye, M. Geletu, A. Abdeldayem, J. Israelian, T. B. Radu, A. Sedighi, M.N. Bhatti, M.M. Hassan, P. Manaswiyoungkul, A. E. Shouksmith, H.A. Neubauer, E.D. de Araujo, T. Aittokallio, O.H. Krämer, R. Moriggl, S. Mustjoki, M. Herling, P.T. Gunning, Development of HDAC inhibitors exhibiting therapeutic potential in T-Cell prolymphocytic leukemia, J. Med. Chem. 64 (12) (2021) 8486–8509, https://doi.org/10.1021/acs.jmedchem.1c00420.

[70] O.O. Olaoye, P.R. Watson, N. Nawar, M. Geletu, A. Sedighi, S. Bukhari, Y. S. Raouf, P. Manaswiyoungkul, F. Erdogan, A. Abdeldayem, A.D. Cabral, M. M. Hassan, K. Toutah, A.E. Shouksmith, J.M. Gawel, J. Israelian, T.B. Radu, N. Kachhiyapatel, E.D. de Araujo, D.W. Christianson, P.T. Gunning, Unique molecular interaction with the histone deacetylase 6 catalytic tunnel: crystallographic and biological characterization of a model chemotype, J. Med. Chem. 64 (5) (2021) 2691–2704, https://doi.org/10.1021/acs.jmedchem.0c01922.

[71] N. Nawar, S. Bukhari, A.A. Adile, Y. Suk, P. Manaswiyoungkul, K. Toutah, O. O. Olaoye, Y.S. Raouf, A. Sedighi, H.K. Garcha, M.M. Hassan, W. Gwynne, J. Israelian, T.B. Radu, M. Geletu, A. Abdeldayem, J.M. Gawel, A.D. Cabral, C. Venugopal, E.D. de Araujo, S.K. Singh, P.T. Gunning, Discovery of HDAC6-Selective inhibitor NN-390 with in vitro efficacy in group 3 medulloblastoma, J. Med. Chem. 65 (4) (2022) 3193–3217, https://doi.org/10.1021/acs.jmedchem.1c01585.

[72] S. Shen, C. Picci, K. Ustinova, V. Benoy, Z. Kutil, G. Zhang, M.T. Tavares, J. Pavlíček, C.A. Zimprich, M.B. Robers, L. Van Den Bosch, C. Bařinka, B. Langley, A.P. Kozikowski, Tetrahydroquinoline-capped histone deacetylase 6 inhibitor SW-101 ameliorates pathological phenotypes in a charcot–marie–tooth type 2A mouse model, J. Med. Chem. 64 (8) (2021) 4810–4840, https://doi.org/10.1021/acs.jmedchem.0c02210.

[73] H.K. Garcha, N. Nawar, H. Sorger, F. Erdogan, M.M. Aung, A. Sedighi, P. Manaswiyoungkul, H.-S. Seo, S. Schönefeldt, D. Pölöske, S. Dhe-Paganon, H. A. Neubauer, S.M. Mustjoki, M. Herling, E.D. de Araujo, R. Moriggl, P.T. Gunning, High efficacy and drug synergy of HDAC6-Selective inhibitor NN-429 in natural killer (NK)/T-Cell lymphoma, Pharmaceuticals 15 (11) (2022) 1321, https://doi.org/10.3390/ph15111321.

[74] A. Kozikowski, J.H. Kalin, K.V. Butler, J. Bergman, W.W. Hancock, Hdac Inhibitors and Therapeutic Methods Using the Same WO2012106343A2, 2012.

[75] M.V. Kozlov, K.A. Konduktorov, A.S. Shcherbakova, S.N. Kochetkov, Synthesis of N'-propylhydrazide analogs of hydroxamic inhibitors of histone deacetylases (HDACs) and evaluation of their impact on activities of HDACs and replication of hepatitis C virus (HCV), Bioorg. Med. Chem. Lett. 29 (16) (2019) 2369–2374, https://doi.org/10.1016/j.bmcl.2019.06.006.

[76] F. Baselious, D. Robaa, W. Sippl, Utilization of AlphaFold models for drug discovery: feasibility and challenges. Histone deacetylase 11 as a case study, Comput. Biol. Med. (2023) 107700, https://doi.org/10.1016/j.compbiomed.2023.107700.

[77] P. Aramsangtienchai, N.A. Spiegelman, B. He, S.P. Miller, L. Dai, Y. Zhao, H. Lin, HDAC8 catalyzes the hydrolysis of long chain fatty acyl lysine, ACS Chem. Biol. 11 (10) (2016) 2685–2692, https://doi.org/10.1021/acschembio.6b00396.

[78] S.M. Gantt, C. Decroos, M.S. Lee, L.E. Gullett, C.M. Bowman, D.W. Christianson, C.A. Fierke, General base-general acid catalysis in human histone deacetylase 8, Biochemistry 55 (5) (2016) 820–832, https://doi.org/10.1021/acs.biochem.5b01327.

[79] Y. Hai, D.W. Christianson, Histone deacetylase 6 structure and molecular basis of catalysis and inhibition, Nat. Chem. Biol. 12 (9) (2016) 741–747, https://doi.org/10.1038/nchembio.2134.

[80] M. Marek, T.B. Shaik, T. Heimburg, A. Chakrabarti, J. Lancelot, E. Ramos-Morales, C. Da Veiga, D. Kalinin, J. Melesina, D. Robaa, K. Schmidtkunz, T. Suzuki, R. Holl, E. Ennifar, R.J. Pierce, M. Jung, W. Sippl, C. Romier, Characterization of histone deacetylase 8 (HDAC8) selective inhibition reveals specific active site structural and functional determinants, J. Med. Chem. 61 (22) (2018) 10000–10016, https://doi.org/10.1021/acs.jmedchem.8b01087.

[81] A. Barducci, M. Bonomi, M. Parrinello, Metadynamics, WIREs Comput. Mol. Sci. 1 (5) (2011) 826–843, https://doi.org/10.1002/wcms.31.

[82] L. Fusani, D.S. Palmer, D.O. Somers, I.D. Wall, Exploring ligand stability in protein crystal structures using binding pose metadynamics, J. Chem. Inf. Model. 60 (3) (2020) 1528–1539, https://doi.org/10.1021/acs.jcim.9b00843.

[83] A.J. Clark, P. Tiwary, K. Borrelli, S. Feng, E.B. Miller, R. Abel, R.A. Friesner, B. J. Berne, Prediction of protein-ligand binding poses via a combination of induced fit docking and metadynamics simulations, J. Chem. Theor. Comput. 12 (6) (2016) 2990–2998, https://doi.org/10.1021/acs.jctc.6b00201.

[84] Schrödinger Release 2019-1, Maestro, Schrödinger, LLC, New York, NY, 2019.

[85] G.M. Sastry, M. Adzhigirey, T. Day, R. Annabhimoju, W. Sherman, Protein and ligand preparation: parameters, protocols, and influence on virtual screening enrichments, J. Comput. Aided Mol. Des. 27 (3) (2013) 221–234, https://doi.org/10.1007/s10822-013-9644-8.

[86] Schrödinger Release 2019-1: Protein Preparation Wizard, Epik, Schrödinger, LLC, New York, NY, 2019. *Impact, Schrödinger, LLC, New York, NY, 2019; Prime, Schrödinger, LLC*, New York, NY, 2019.

[87] Schrödinger Release 2019-1, Epik, Schrödinger, LLC, New York, NY, 2019.

[88] J.R. Greenwood, D. Calkins, A.P. Sullivan, J.C. Shelley, Towards the comprehensive, rapid, and accurate prediction of the favorable tautomeric states of drug-like molecules in aqueous solution, J. Comput. Aided Mol. Des. 24 (6–7) (2010) 591–604, https://doi.org/10.1007/s10822-010-9349-1.

[89] J.C. Shelley, A. Cholleti, L.L. Frye, J.R. Greenwood, M.R. Timlin, M. Uchimaya, Epik: a software program for pK(a) prediction and protonation state generation for drug-like molecules, J. Comput. Aided Mol. Des. 21 (12) (2007) 681–691, https://doi.org/10.1007/s10822-007-9133-z.

[90] Schrödinger Release 2019-1, LigPrep, Schrödinger, LLC, New York, NY, 2019.

[91] Schrödinger Release 2019-1: Glide, Schrödinger, LLC, New York, NY, 2019.

[92] R.A. Friesner, J.L. Banks, R.B. Murphy, T.A. Halgren, J.J. Klicic, D.T. Mainz, M. P. Repasky, E.H. Knoll, M. Shelley, J.K. Perry, D.E. Shaw, P. Francis, P.S. Shenkin, Glide: a new approach for rapid, accurate docking and scoring. 1. Method and assessment of docking accuracy, J. Med. Chem. 47 (7) (2004) 1739–1749, https://doi.org/10.1021/jm0306430.

[93] R.A. Friesner, R.B. Murphy, M.P. Repasky, L.L. Frye, J.R. Greenwood, T. A. Halgren, P.C. Sanschagrin, D.T. Mainz, Extra precision glide: docking and scoring incorporating a model of hydrophobic enclosure for protein-ligand complexes, J. Med. Chem. 49 (21) (2006) 6177–6196, https://doi.org/10.1021/jm051256o.

[94] T.A. Halgren, R.B. Murphy, R.A. Friesner, H.S. Beard, L.L. Frye, W.T. Pollard, J. L. Glide Banks, A new approach for rapid, accurate docking and scoring. 2. Enrichment factors in database screening, J. Med. Chem. 47 (7) (2004) 1750–1759, https://doi.org/10.1021/jm030644s.

[95] W.L. Jorgensen, D.S. Maxwell, J. Tirado-Rives, Development and testing of the OPLS all-atom force field on conformational energetics and properties of organic

liquids, J. Am. Chem. Soc. 118 (45) (1996) 11225–11236, https://doi.org/10.1021/ja9621760.
[96] W.L. Jorgensen, J. Tirado-Rives, The OPLS [optimized potentials for liquid simulations] potential functions for proteins, energy minimizations for crystals of cyclic peptides and crambin, J. Am. Chem. Soc. 110 (6) (1988) 1657–1666, https://doi.org/10.1021/ja00214a001.
[97] E. Harder, W. Damm, J. Maple, C. Wu, M. Reboul, J.Y. Xiang, L. Wang, D. Lupyan, M.K. Dahlgren, J.L. Knight, J.W. Kaus, D.S. Cerutti, G. Krilov, W.L. Jorgensen, R. Abel, R.A. Friesner, OPLS3: a force field providing broad coverage of drug-like small molecules and proteins, J. Chem. Theor. Comput. 12 (1) (2016) 281–296, https://doi.org/10.1021/acs.jctc.5b00864.
[98] D. Shivakumar, J. Williams, Y. Wu, W. Damm, J. Shelley, W. Sherman, Prediction of absolute solvation free energies using molecular dynamics free energy perturbation and the OPLS force field, J. Chem. Theor. Comput. 6 (5) (2010) 1509–1519, https://doi.org/10.1021/ct900587b.
[99] Schrödinger Release 2019-1, Desmond Molecular Dynamics System, D.E. Shaw Research, New York, NY, USA, 2019. Maestro-Desmond Interoperability Tools, Schrödinger: New York, NY, USA, 2019.
[100] K.J. Bowers, D.E. Chow, H. Xu, R.O. Dror, M.P. Eastwood, B.A. Gregersen, J. L. Klepeis, I. Kolossvary, M.A. Moraes, F.D. Sacerdoti, J.K. Salmon, Y. Shan, D. E. Shaw, Scalable algorithms for molecular dynamics simulations on commodity clusters, in: SC '06: Proceedings of the 2006 ACM/IEEE Conference on Supercomputing, 2006, https://doi.org/10.1109/SC.2006.54, pp. 43–43.
[101] Schrödinger Release 2019-1: Qikprop, Schrödinger, LLC, New York, NY, 2019.
[102] Schrödinger Release 2019-1: Canvas, Schrödinger, LLC, New York, NY, 2019.
[103] J. Duan, S.L. Dixon, J.F. Lowrie, W. Sherman, Analysis and comparison of 2D fingerprints: insights into database screening performance using eight fingerprint methods, J. Mol. Graph. Model. 29 (2) (2010) 157–170, https://doi.org/10.1016/j.jmgm.2010.05.008.
[104] S. Zhang, A. Golbraikh, S. Oloff, H. Kohn, A. Tropsha, A novel automated lazy learning QSAR (ALL-QSAR) approach: method development, applications, and virtual screening of chemical databases using validated ALL-QSAR models, J. Chem. Inf. Model. 46 (5) (2006) 1984–1995, https://doi.org/10.1021/ci060132x.
[105] A. Tropsha, P. Gramatica, V.K. Gombar, The importance of being earnest: validation is the absolute essential for successful application and interpretation of QSPR models, QSAR Comb. Sci. 22 (1) (2003) 69–77, https://doi.org/10.1002/qsar.200390007.
[106] B.I. Tingle, K.G. Tang, M. Castanon, J.J. Gutierrez, M. Khurelbaatar, C. Dandarchuluun, Y.S. Moroz, J.J. Irwin, ZINC-22—A free multi-billion-scale database of tangible compounds for ligand discovery, J. Chem. Inf. Model. 63 (4) (2023) 1166–1176, https://doi.org/10.1021/acs.jcim.2c01253.
[107] M. Zessin, Z. Kutil, M. Meleshin, Z. Nováková, E. Ghazy, D. Kalbas, M. Marek, C. Romier, W. Sippl, C. Bařinka, M. Schutkowski, One-atom substitution enables direct and continuous monitoring of histone deacylase activity, Biochemistry 58 (48) (2019) 4777–4789, https://doi.org/10.1021/acs.biochem.9b00786.
[108] T. Heimburg, F.R. Kolbinger, P. Zeyen, E. Ghazy, D. Herp, K. Schmidtkunz, J. Melesina, T.B. Shaik, F. Erdmann, M. Schmidt, C. Romier, D. Robaa, O. Witt, I. Oehme, M. Jung, W. Sippl, Structure-based design and biological characterization of selective histone deacetylase 8 (HDAC8) inhibitors with anti-neuroblastoma activity, J. Med. Chem. 60 (24) (2017) 10188–10204, https://doi.org/10.1021/acs.jmedchem.7b01447.